Teneurin-3 and latrophilin-2 are required for somatotopic map formation and somatosensory topognosis

Kevin T. Sangster[1,2], Xinying Zhang[1,2], Daniel del Toro[3], Christina Sarantopoulos[1,2], Ashley M. Moses[4], Shreya Mahasenan[1], Daniel T. Pederick[4], Sophie Perreault[5], Catherine Fallet-Bianco[6,7], R. Brian Roome[8], Elena Seiradake[9], Liqun Luo[4], Artur Kania[1,2,10,11 *]

Affiliations:

[1]Institut de Recherches Cliniques de Montréal (IRCM), Montréal, QC, Canada, [2]Integrated Program in Neuroscience, McGill University, Montréal, QC, Canada, [3]Department of Biomedical Sciences, Faculty of Medicine and Health Sciences, Institute of Neurosciences, IDIBAPS, CIBERNED, University of Barcelona, Barcelona, Spain, [4]Department of Biology, Howard Hughes Medical Institute, Stanford University, Stanford, CA, USA, [5]Azrieli Research Center at CHU Sainte-Justine, Montréal, QC, Canada, [6]Department of Pathology, CHU Sainte-Justine, Montréal, QC, Canada, [7]Department of Pathology and Cell Biology, Université de Montréal, Montréal, QC, Canada [8]Spinal Circuits and Plasticity Unit, National Institute of Neurological Disorders and Stroke, Bethesda, MD, USA, [9]Department of Biochemistry, Oxford University, Oxford, UK, [10]Division of Experimental Medicine, McGill University, Montréal, QC, H3A 2B2, Canada, [11]Department of Anatomy and Cell Biology, McGill University, Montréal, QC, H3A 0C7, Canada

***Corresponding author. Email: artur.kania@ircm.qc.ca**

Abstract:

Somatotopy is a recurring organizational feature of the somatosensory system where adjacent neurons and their connections represent adjacent regions of the body. The molecular mechanisms governing the formation of such “body maps” remain largely unknown. Here we demonstrate that the cell surface proteins teneurin-3 and latrophilin-2 are expressed in opposing gradients in multiple somatotopic maps in the mouse, including within the dorsal horn of the spinal cord. Genetic manipulation of these proteins in spinal dorsal horn or sensory neurons distorts the somatotopy of neuronal connections and impairs accurate localisation of a noxious stimulus on the surface of the body. Our work provides the foundation for a molecular model of somatotopic map formation and insights into their function in localisation of somatosensory stimuli or topognosis.

Introduction

The structure of neuronal connections can reveal their functional logic. One of the organising principles of neuronal circuits are "topographic maps" which maintain the spatial relationship between a group of neurons and their post-synaptic targets. The consequence of this in the context of sensory processing is that information concerning adjacent stimuli is communicated by adjacent neurons at multiple levels of a sensory system. The classical system for studying the development of such maps has been the retinotopic map, where it has been shown that map formation is driven by specific cell surface effectors of neuronal connectivity and refinement by neuronal activity (*1–8*). However, our understanding of the development of other sensory maps, particularly in the somatosensory system, remains limited.

Somatotopic maps are a unique example of topographic maps where nearby neurons represent contiguous anatomical structures. Somatotopic organization is characteristic of most vertebrate somatosensory regions, including but not limited to the dorsal horn of the spinal cord (DH) (*9–11*), dorsal column nuclei (*12–14*), ventrobasal thalamus (*15*, *16*), and primary somatosensory cortex (*17*, *18*). The rodent DH exhibits a rostrocaudal organization that corresponds to the dermatomes organised along the rostrocaudal axis of the body, as well as a mediolateral (ML) organisation that corresponds to the proximodistal (PD) axis of the body (*9–11*). The medial dorsal horn receives sensory inputs from distal regions (e.g. the paw), while the lateral dorsal horn corresponds to more proximal regions of the body (e.g. the shoulder/hip to midline). The ML map is oriented orthogonally to the dorsal horn laminae that receive modality-specific sensory afferents (*19*, *20*); the result is a columnar-like architecture where a vertical "columel" processes noxious, thermal and light touch information originating in a particular PD zone on the surface of the limb (*21*, *22*). This somatotopic map has been thoroughly demonstrated both in terms of neuronal activity induced by sensory stimuli (*22–27*), and in terms of the organisation of incoming sensory afferents (*10*, *11*, *28*).

Despite the discovery of somatotopic maps over a century ago and much speculation as to their role in internal representation of our bodies, the mechanisms that underly their development remain poorly

55 understood (*17*, *29–31*). It is known that neuronal activity plays a critical role in the refinement of
56 developing ST maps (*32–34*). On the other hand, afferent sensory axons show an somatotopic organization
57 upon entry in the DH, suggesting a contribution by hard-wiring molecular signals (*28*, *35–38*). However,
58 the identity of such cues has remained elusive: none of the classical neuronal connectivity molecules appear
59 to be involved despite their extensive study. Here, we identify cell surface proteins teneurin-3 (Ten3) and
60 latrophilin-2 (Lphn2) as being essential cues for the formation of the DH somatotopic map.

61

62 **Ten3 and Lphn2 expression reflects the ST organization of the DH**

63 Recent work has shown that heterophilic repulsion Ten3 and Lphn2, in combination with Ten3-
64 Ten3 homophilic attraction, establish a point-to-point topography of neuronal connections in the
65 hippocampus (*39–41*). To determine whether Lphn2 and Ten3 could direct the development of DH
66 connectivity, we examined their expression in the mouse lumbar DH at embryonic day 14.5 (e14.5), when
67 cutaneous afferents begin their entry into spinal laminae I through IV (*42*, *43*). There, we observed
68 complementary mRNA gradients that spanned the limb somatotopic map: *Lphn2* mRNA expression was
69 high in the medial DH (subserving the distal limb) but low in the lateral DH, while *Ten3* mRNA expression
70 was high in the lateral DH (subserving the proximal limb), but low in the medial DH (Fig. 1 A). Analysis
71 of protein expression using an anti-Ten3 antibody (*39*) and *Lphn2-mVenus* knock-in mice (*44*) revealed
72 similar mediolateral gradients (Fig. 1B).

73 Although there is no somatotopic organisation of DRG neurons at the level of individual ganglia,
74 their anterio-posterior position correlates with the identity of the dermatome innervated by them (*9*, *45*, *46*).
75 In DRG neurons we observed widespread expression of *Ten3* and *Lphn2* in all major sensory neuron
76 subtypes (Fig. S1A). However, we did not observe any spatial bias to *Ten3* or *Lphn2* expression in individual
77 ganglia along either the dorsoventral or mediolateral axes (Fig. S1B). On the other hand, we did observe an
78 inverse relationship between *Ten3* and *Lphn2* mRNA levels in individual DRG neurons, where those that

79 expressed a high level of *Ten3* mRNA, also expressed low levels of *Lphn2* and vice versa (Fig. S1C).
80 Additionally, reflecting the dermatome organisation, ganglia enriched in distal hindpaw-innervating
81 neurons, such as L3-5, tended to have high *Lphn2* and low *Ten3* levels of expression. Conversely, ganglia
82 enriched in more proximally-projecting neurons, such as L1-2 and L6, tended to have low Lphn2 and high
83 Ten3 levels of expression (Fig. 1C). Thus, the level of sensory neuron expression of Lphn2 and Ten3
84 correlated with DH Lphn2 and Ten3 gradients and the somatotopic map of limb: distal limb sensory neurons
85 expressing high *Lphn2* levels innervated the proximal DH region expressing low levels of Ten3, and those
86 sensory neurons that expressed high levels of Ten3 innervated the distal DH regions expressing low Lphn2
87 levels. A similar correlation could be made between the protein gradients in the DRG axons located in the
88 dorsal root entry zone (DREZ) immediately outside the DH and the gradients in the DH (Fig. 1B and S1D).
89 Next, to identify if Ten3 and Lphn2 gradients align with somatotopic maps in other somatosensory regions,
90 we examined *Ten3* and *Lphn2* expression in the ventrobasal (VB) thalamus (postsynaptic to projection
91 neurons in the DH) and uncovered a similar gradient that aligned with the VB somatotopic map (Fig. S1E).
92 Finally, to examine whether such Ten3/Lphn2 gradients are evolutionarily conserved we examined the
93 expression of *TENM3* and *ADGRL2* mRNAs, encoded by the human homologues of mouse Ten3 and
94 Lphn2, in the human fetal dorsal horn (Fig. S1F). Therefore, *Ten3* and *Lphn2* are expressed in gradients
95 along the proximodistal axis of somatotopic maps in a conserved manner across the somatosensory system.

96

97 **Ten3 and Lphn2 are required for the somatotopy of sensory afferents**

98 Based on the observed expression patterns in the DH and DRG, as well as the previously described
99 functions of these proteins (*40*), we hypothesized the following (Fig. 1D): (1) repulsion from Ten3 in the
100 DH acting on Lphn2 in DRG axons directs distal limb afferents to the medial DH, (2) a combination of
101 repulsion from Lphn2 in the medial DH acting on Ten3 in the DRG axons and attraction from Ten3 in the
102 lateral DH acting on Ten3 in DRG axons cooperate to direct proximal limb afferents to the lateral DH. To
103 test our hypothesis, we first challenged DRG axons with a purified $Lphn2^{Lec}$ (lectin domain) and Ten3

proteins. We found that both Lphn2^{Lec} and Ten3 are repulsive to DRG axons *in vitro* (Fig. S2), thereby demonstrating that Ten3 and Lphn2 are capable of guiding DRG axons *in vitro*. We then generated conditional knockouts (cKOs) of *Ten3* and *Lphn2* in the DRG and DH (Fig. S3A, methods), hereby referred to as Ten3$^{\Delta DRG}$, Lphn2$^{\Delta DRG}$, Ten3$^{\Delta DH}$, and Lphn2$^{\Delta DH}$. To assess the distribution of sensory afferents along the mediolateral extent of the DH, we co-injected cholera toxin subunit B (CTB) and wheat germ agglutinin (WGA) subcutaneously, which preferentially label myelinated and unmyelinated sensory afferents, respectively (*11*, *34*, *47*). This allowed us to examine the targeting of superficial versus deep (SD) DH of unmyelinated afferents which convey pain and thermal information and innervate the superficial DH laminae, from myelinated afferents which convey innocuous touch information and innervate deeper DH laminae. We are also able to assess the alignment of these two classes of inputs along the mediolateral axis.

We first examined distal limb afferent inputs to the DH, which we hypothesized to be guided by Ten3 (DH) → Lphn2 (DRG) repulsion. We therefore examined these afferents in Ten3$^{\Delta DH}$ and Lphn2$^{\Delta DRG}$ cKO mice compared to littermate controls by injecting CTB/WGA into the hindpaw and quantified the distribution of the labelled axons along the ML and SD axes of the DH (Fig. S3B). In wild-type mice, the paw representation is disproportionally large and duplicated at the most medial extreme of the dorsal horn (*11*, *22*, *34*, *48*). In our controls, we saw the expected wild-type distribution of afferents but in Ten3$^{\Delta DH}$ cKO mice we observed a dramatic shift in the ML distribution of afferents (Fig. 2A-C, S3C). Meanwhile, CTB and WGA-labelled axons remained in register along the ML axis (Fig. S3D), and there was no shift in the distribution of CTB and WGA-labelled axons along the orthogonal SD axis (Fig. S3E-G). The Lphn2$^{\Delta DRG}$ cKO mice exhibited a milder but significant shift along the ML axis and no change in the SD axis distribution or in the ML alignment between CTB and WGA-labelled afferents (Fig. 2D-F, S3H-L).

We next examined proximal afferent inputs to the DH, which we hypothesize are guided by a combination of Lphn2 (DH) → Ten3 (DRG) repulsion and Ten3 (DH) → Ten3 (DRG) attraction. We therefore examined these afferents in Ten3$^{\Delta DH}$, Lphn2$^{\Delta DH}$, and Ten3$^{\Delta DRG}$ cKO mice and compared them to littermate controls by injecting CTB/WGA subcutaneously at the dorsal midline. Like for the distal limb

afferents, we observed a dramatic shift in the ML distribution of proximal afferents in the Ten3$^{\Delta DH}$ cKO mice (Fig. 3A-C, S4A). However, this was accompanied by a decrease in the ML alignment of the CTB with the WGA-labelled afferents (Fig. S4B), and an expansion in the SD distribution of both classes of afferents (Fig. S4C-E). Lphn2$^{\Delta DH}$ cKO mice exhibited a comparatively mild but significant shift along the ML and SD axes, without a consequence on the alignment of CTB with the WGA-labelled afferents (Fig. 3D-F, S4F-J). Unexpectedly, the Ten3$^{\Delta DRG}$ cKO mice did not exhibit any significant changes in the targeting of afferents in the DH (Fig. 3G-I, S4K-O), indicating that Ten3 in the DRG may be dispensable for correct somatotopic and laminar targeting. Importantly, Ten3 (DH) → Lphn2 (DRG) repulsion is likely intact in Ten3$^{\Delta DRG}$ cKO mice, suggesting that this repulsion alone may be sufficient to separate the distal and proximal inputs along the ML axis. Together, our cKO experiments demonstrate that Ten3 and Lphn2 are essential for the correct somatotopic organization of primary sensory afferents in the DH, with the severity of miswiring phenotypes that depended on the ablated gene and targeted tissue.

Computational modelling of somatotopic map formation in the DH

To better understand our observed phenotypes and gain further insights into the developmental programs that produce the DH somatotopic map, we sought to develop a comprehensive computational model of DH somatotopic map formation. Over the past 40 years, several computational models of topographic map formation in the visual system have been developed and iteratively improved with experimental data. We first sought to determine if these theoretical models of topographic map formation could be applied to somatotopic maps. We therefore adapted the Koulakov model (*8*, *49*, *50*) (see methods) as it is a relatively abstract model without excessive constraints regarding the cellular mechanisms. It also effectively predicts the observed effects of genetic manipulations (*51*), and incorporates guidance cues, competition, and activity-dependent refinement into a single unified model (*8*). After adapting this model to the DH somatotopic map, we then performed Bayesian Simulation-Based Inference (SBI) using the Sequential Monte Carlo method for Approximate Bayesian Computation (ABC-SMC) to identify parameter

values for our model that fit both the observed control and cKO data in an unbiased manner (Fig. 4A; see methods).

We first confirmed that this model was able to accurately reproduce the proximal → lateral and distal → medial connectivity between DRG and DH neurons under wild-type conditions (Fig. 4B and Fig. S5A). We then confirmed we were able to closely recapitulate the observed distributions of CTB/WGA along the ML axis in both controls and all cKOs examined experimentally above (Fig. 4C). Inspection of the parameter values (Table S1) reveals that the best fitting model incorporates a prominent role for activity-dependent refinement of connectivity, consistent with previous experimental results (*32–34*). Our model also indicates that there is strong competition between DRG axons for limited space in the DH along the ML axis, consistent with previous results showing an expansion of the saphenous nerve afferent termini when the afferents of the sciatic nerve are eliminated (*52*, *53*). We recreated this experiment *in silico* by ablating proximal limb DRG neurons in our model and observed a similar expansion of the remaining axons to fill the available ML extent of the DH (Fig. S5B, C). Additional inferences of our model are that Ten3 (DH) → Lphn2 (DRG) repulsion plays a more prominent role than Lphn2 (DH) → Ten3 (DRG) repulsion or Ten3 (DH) → Ten3 (DRG) attraction, and that there is an effect on both guidance and activity-dependent refinement, particularly in the Ten3$^{\Delta DH}$ cKOs. Taken together, despite being developed for a different sensory system being patterned by unrelated molecular cues, theoretical models of topographic map formation in the visual system can be applied to developing somatotopic maps. We also show that our observed cKO data are consistent with the model that gradients of Ten3/Lphn2 cooperate to specify the DH somatotopic map.

Ten3$^{\Delta DH}$ cKOs exhibit an altered somatotopic distribution of neural activity and behavioural responses

177 Given the observed miswiring phenotypes, we sought to examine if this miswiring was
178 accompanied by alterations in the function of DH circuitry. Towards this end, we selected the cKO with the
179 most severe miswiring phenotype (Ten3$^{\Delta DH}$) and examined the consequence of injection the hindpaw with
180 formalin, a noxious stimulus that causes a somatotopically restricted induction of the neuronal activity
181 proxy marker Fos in DH neurons (*23*). Following injection of formalin into the distal regions of the
182 hindpaw, both Ten3$^{\Delta DH}$ cKO mice and control littermates displayed a significant induction of Fos expression
183 in the DH ipsilateral to the injection (Fig. S6A, B). While the control littermates showed increased Fos
184 expression predominantly in the somatotopically appropriate medial region of the DH, in line with the
185 innervation pattern from distal limb DRG afferents, the Ten3$^{\Delta DH}$ cKO mice exhibited a greater number of
186 Fos-expressing cells in the lateral DH (Fig. 5A-D). Matching the more widespread induction of Fos, cKO
187 mice also had more Fos-expressing cells overall on the side ipsilateral to the injection when compared to
188 control littermates (Fig. S6C-E).

189 In addition to being able to induce somatotopically restricted Fos activity, formalin injection into
190 the glabrous skin of the paw, i.e., the distal hindlimb, elicits highly accurate licking of the injected site.
191 Thus, using this paradigm we sought to examine the functional impact of somatotopic miswiring on the
192 ability to locate a stimulus on the surface of the body, or topognosis. We first examined the precision of
193 topognosis in Ten3 constitutive knockout (Ten3^{KO}) mice (*39*, *54*). Compared to control littermates, Ten3^{KO}
194 mice spent less time licking regions of the limb close to the injection site and more time licking regions of
195 the limb farther from the injection (Fig. S6F,G), potentially indicating a deficit in their ability to precisely
196 locate the stimulus. Meanwhile, the duration of licking, an indication of stimulus intensity, was not different
197 between KO and control mice (Fig. S6H). However, Ten3^{KO} mice also showed defects in the ability to
198 remove an adhesive tape placed on their hindlimbs, suggesting broad deficits in sensorimotor coordination
199 (Fig. S6I,J). We next assessed topognosis in Ten3$^{\Delta DH}$ cKO mice given the magnitude of their anatomical
200 miswiring phenotype. Similar to the Ten3^{KO} mice, Ten3$^{\Delta DH}$ cKO mice exhibited a reduction in time spent
201 licking areas close to the injection and increase in time licking areas farther from the injection site (Fig. 5E,

202 S6L), indicating they also had showed impaired topognosis. Again, this phenotype was not accompanied
203 by any significant changes in licking duration (Fig. S6K). Finally, unlike the Ten3^{KO} mice, Ten3$^{\Delta DH}$ mice
204 performed normally in the adhesive removal assay (Fig. S6M,N), indicating a lack of defects in
205 sensorimotor coordination.

206

207 **Discussion**

208 Our study provides foundational insights into the molecular logic of somatotopic map formation.
209 First, our experimental observations and modelling argue that the somatotopic map formed between
210 peripheral sensory neurons and those endogenous to the spinal DH is driven by graded expression of Ten3
211 and Lphn2. This complements previous studies on their role in establishing of neuronal connections through
212 their binary or all-or-nothing attractive and repulsive signalling. Additionally, we also provide direct
213 functional evidence of the importance of somatotopic maps in the localisation of a stimulus on the surface
214 of the skin.

215 Several parallels and distinctions between our work and that on the formation of retinotopic
216 connectivity can also be made. Like in retinotopic maps, past studies and this work suggest that axon-axon
217 interactions such as pre-ordering prior to arrival in target area and inter-axon competition, as well as
218 activity-dependent refinement, play an important role in the establishment of the DH somatotopic map.
219 However, the nature of the miswiring phenotypes observed by us differs significantly from those following
220 Eph/ephrin signalling manipulations in the retinocollicular system. While Eph/ephrin signalling loss largely
221 result in the formation of additional compact terminal zones of retinal axons in the superior colliculus (*4*,
222 *5*, *55*), we generally observe broadening of sensory axon terminal zones in the ML axis of the DH, without
223 the formation of any additional ones, suggesting fundamental cellular/molecular differences between these
224 processes. Of particular interest would be the significance of Ten3/Lphn2 and Eph/ephrins gradient co-
225 expression, the latter of which has been implicated in somatosensory cortex somatotopic map formation
226 afferent thalamic axon connectivity (*56*, *57*). Finally, the presence of Ten3/Lphn2 gradients in many regions

227 of the developing nervous system raises the possibility that they pattern all somatotopic maps within the
228 somatosensory system, and more generally, circuits whose organising principle requires the preservation of
229 spatial relationship between neurons and their targets (*58*).

230 Although we cannot rule out other DH functions of Ten3 contributing to the impaired topognosis
231 phenotype, the unchanged licking duration in Ten3$^{\Delta DH}$ cKOs suggests that stimulus intensity and location
232 can be dissociated, echoing the idea of parallel motivational/affective and discriminatory systems
233 underlying nociception (*59*). Importantly, our data provide some of the only functional evidence
234 supporting the importance of somatotopic maps in somatosensory function. Penfield's original
235 experiments involved stimulating cortical neurons and do not allow any inferences regarding the
236 requirement of somatotopic maps (*17*). Our genetics-based precise manipulation of a somatotopic map
237 provides a new potential inroad into questions such as map plasticity, the integration of somatotopic
238 somatosensory maps with somatotopic motor maps, or those of other sensory modalities, and their overall
239 function in representing our bodies and whole body action planning (*31*).

240

Acknowledgments: We thank Meirong Liang for technical support; the IRCM animal facility staff; Drs. Jeffrey Mogil and Samantha Butler for comments on the manuscript; Dr. Farin Bourojeni and other members of the Kania laboratory for advice, feedback, and support. **Funding:** This work was supported by project grants from the Canadian Institutes of Health Research (CIHR; PJT-162225, MOP-77556, PJT-153053, PJT-159839, and PJT-197987) to AK and National Institutes of Health (NIH; R01-NS050580) to LL. AK holds the Doggone Foundation Chair of Excellence in Pain and receives support from the Fondation IRCM. KTS is a recipient of a CIHR doctoral scholarship (FRN:494078). XZ is a recipient of a Fonds de recherche du Québec -Santé doctoral scholarship. **Author contributions:** K.T.S. Performed all experiments except for the *in-vitro* and behavioural experiments, analyzed the data, and performed the computational modelling. The *in-vitro* experiments were performed and analyzed by D.d.T. with reagents generated by E.S. Behavioural experiments using Ten3^{KO} mice were performed by A.M.M. and D.T.P. and quantified by S.M. Behavioural experiments using Ten3^{DH} mice were performed by X.Z. and quantified by C.S. R.B.R contributed to investigation and conceptualization. L.L., S.P., T.B. and C.F.B. provided reagents. A.K. supervised the study and acquired funding. A.K. and K.T.S. wrote the paper. **Ethics:** All vertebrate animal experiments were carried out in accordance with the Canadian Council on Animal Care guidelines and approved by the IRCM Animal Care Committee (Protocol 2023-11 AK and 2021-12 AK). **Competing interests:** The authors declare no competing financial interests. **Data and materials availability:** All data are available in the main paper and supplementary materials. All materials are available through requests to the corresponding author.

265 **Materials and Methods:**

266 **Acquisition of human tissue:** Collection of the human fetal spinal cord samples were with the parent's
267 written informed consent. They were obtained through a spontaneous or induced abortion donor program
268 at the Centre hospitalier universitaire - Sainte-Justine (CHU-SJ), approved by the IRCM and CHU-SJ
269 Research Ethics Committee under the name "Pour une meilleure compréhension du développement de la
270 moelle épinière et des maladies qui y sont associées". Donor spinal cords were dissected and fixed for 24h
271 in formalin, then processed for cryosectioning as below.

272 **Mouse lines:** All animal studies were approved by the IRCM's Animal Care Committee in agreement with
273 Canadian Council on Animal Care (CCAC) guidelines, as per protocol numbers 2021-12AK and 2023-
274 11AK. Mice were group housed with access to food and water *ad libitum*. All mice were maintained on a
275 mixed C57BL/6 and 129/Sv background and mixture of both male and female mice were used for all
276 experiments. All experiments were done using littermate controls. Mouse lines used in this study include
277 *Lbx1:Cre* (*60*), *PLAT:Cre* (*61*), *Ten3*^{fl} (*39*), *Lphn2*^{fl} (*44*) and *Ten3*^{KO} (*54*). Within the spinal cord, *Lbx1:Cre*
278 drives recombination within the dI4/dILA, dI5/dILB populations which make up the majority of the dorsal
279 horn while sparing most other spinal populations and the DRG (*62–64*). Meanwhile, *PLAT:cre* targets
280 neural crest derived cells, including the neurons of the DRG, while sparing the spinal cord and brain (*61*).
281 *PLAT:Cre* was chosen over alternatives like *Pirt:Cre* and *Advilin:Cre* since it is expressed in neural crest-
282 derived cells as early as Theiler Stage 15 (e9.5) and is widespread throughout DRG neurons by e11.5 (Fig.
283 S2A).

284 **Cutaneous CTB/WGA injections:** Adult mice (>8 weeks old) were anaesthetised via continuous
285 inhalation of isofluorane (1-3%) and injected with 4 µl of a mixture of 5 mg/ml CTB-AF488 (Thermo,
286 C34775) and 20 mg/ml WGA-AF555 (Thermo, W32464) dissolved in sterile PBS. Blunt forceps were
287 used to pinch and stabilize the skin and injections were performed into the dermis using a beveled glass
288 capillary needle. Distal injections were performed to the glabrous skin of the hindpaw between the two
289 distal-most promontories. Proximal injections were performed at the dorsal midline at the same

290 rostrocaudal level as the iliac crest. All mice were perfused after three days following the injection as
291 described below.

292 **Formalin Assay and Fos induction:** The formalin assay was performed as previously described (*65–67*).
293 Mice were first habituated to the testing chamber (a clear plastic cylinder filmed from below). They were
294 then subcutaneously injected with 20 µl of 2% formalin (in 0.9% saline) to the plantar surface of the hind
295 paw using a 28G needle and returned to the chamber. Video was recorded from below for 60 minutes
296 following injection. Time spent licking each region of the body was quantified in both the acute (0-10
297 minutes after injection) and chronic phase (11-60 minutes). Mice were then anesthetized and, after an
298 additional 30 minutes, perfused as described below to analyze the distribution of Fos protein (after a total
299 of 90 minutes following the stimulus).

300 **Tissue fixation, freezing and sectioning:** Mice were anesthetized via intraperitoneal injection of a
301 Ketamine/Xylazine mixture (0.1ml/g body weight of 10 mg/ml Ketamine, 1 mg/ml Xyaline, in 0.9%
302 saline). Mice were then perfused with approximately 15 ml of 1x PBS followed by 15 ml of 4% PFA in
303 PBS. Brains and spinal cords were post-fixed in 4% PFA overnight, washed 3x with PBS and left in a
304 30% sucrose in PBS solution until they had sunk. Tissue was cryosectioned into 25 µm sections for adult
305 tissue used for immunohistochemistry and 12 µm sections for embryonic tissue and adult tissue used for
306 RNAscope.

307 **DRG explant culture on Ten3/Lphn2 stripes:** DRG explants from E15.5 embryos were dissected out and
308 plated on 6 cm dishes. Coating was performed using 20 µg/ml laminin and either (1) 50 µg/ml of FC or
309 Lphn2 ectodomain or (2) 50 µg/ml of FC or Ten3 ectodomain. Explants were then cultured for 1-3 days *in*
310 *vitro* at 37°C, 5% CO_2 in Neurobasal medium plus B27 supplement with the addition of 20ng/ml NGF and
311 10ng/ml GDNF. Samples were then fixed with 4% paraformaldehyde for 10 minutes and processed for
312 immunostaining.

313 **Immunohistochemistry:** Tissue sections were washed three times with 1x PBS for 5 minutes, blocked for
314 30 minutes using a solution of 5% heat-inactivated horse serum (HIHS) and 0.1% Triton X-100 in PBS
315 (0.1% tPBS). They were then incubated primary antibody solution (primary antibody in 1% HIHS, 0.1%
316 tPBS) overnight and washed three times with 1x PBS for 5 minutes before being incubated with a secondary
317 antibody (in 1% HIHS, 0.1% tPBS) for 1 hour at room temperature, washed three more times with 1x PBS
318 for 5 minutes, and counterstained with DAPI. Slides were coverslipped using a solution of 10% Mowiol
319 (Sigma) and 25% glycerol, then allowed to dry in the dark prior to imaging.

320 **RNAscope ISH and analysis:** RNAscope *in situ* hybridization was performed according to the
321 manufacturer's protocol using the RNAscope multiplex fluorescent reagent kit (ACDbio cat. no. 323100).
322 Probes used were Mm-Tenm3-C1 (ACDbio, Cat # 411951) and Mm-Lphn2-C2 (ACDbio, Cat #319341-
323 C2). RNAscope images were quantified using QuPath bioimage analysis software (*68*). Nuclear
324 segmentation was performed using StarDist (*69*) and individual puncti and clusters were identified using
325 the QuPath subcellular object detection pipeline. Subcellular detection counts associated with individual
326 cells and their associated coordinates were exported from QuPath and analyzed further in R. The x
327 coordinate location of each cell (mediolateral position) was remapped to a 100-unit standard space and
328 counts for a cells within a given area were binned and visualized as mean counts per cell ± one standard
329 error.

330 **CTB and WGA Image analysis:** Initial preprocessing of images from CTB/WGA injections was
331 performed using Fiji (version 2.14.0/1.54f). Images were first cropped to the dorsal horn up until lamina V
332 and an outline was manually drawn to indicate the region of interest (ROI). For analyses of both tracers,
333 the two channels were first merged using the imageCalculator "Add" function. Fluorescence intensity from
334 all channels were scaled using "Enhance Contrast" with "saturated=0.1" before being thresholded using the
335 auto threshold method "MaxEntropy dark". Preprocessed images and manually drawn ROIs were then
336 further analyzed in R. To account for the curvature of the dorsal horn (with laminae curved downward

337 almost 90 degrees at the lateral extreme), pixel coordinates within each ROI were remapped to a set of
338 anatomical coordinates according to the following functions:

339 $$f_{ML}(x,y) = \begin{cases} x, & x \leq max(x)/2 \\ \tan^{-1}((x - x_0)/(y - y_0)), & x > max(x)/2 \end{cases}$$

340 for mapping x and y pixel coordinates to ML coordinates, and

341 $$f_{SD}(x,y) = \begin{cases} y, & x \leq max(x)/2 \\ \sqrt[2]{(x - x_0)^2 + (y - y_0)^2}, & x > max(x)/2 \end{cases}$$

342 for mapping x and y pixel coordinates to SD coordinates. Where (x_0, y_0) is the origin, with x_0 set at the
343 midpoint of the ROI and y_0 set at the lamina IV/V border for f_{SD} and the lamina V/VI border for f_{ML}. Note
344 that $max(x)$ refers to the maximum x coordinate within the ROI not the whole image. ML and SD
345 coordinates were then normalized to between 0 and 1. Representative examples of these remapped
346 coordinates are provided here (Fig. S2B). The DH was then divided into 50 bins along the ML or SD axes.
347 Since the bins are created based on distance along the given axis, they are not necessarily of equal size (also
348 given the unevenness of the DH) and so the fluorescence intensity is first normalized to bin area, then
349 rescaled to be between 0 and 100 for each image.

350 **Fos image analysis:** Counts of Fos-positive cells was performed manually using the Cell Counter plugin
351 for Fiji (version 2.14.0/1.54f) and xml files containing the coordinates of each marker were exported for
352 further processing in R. Marker coordinates were remapped to standardized anatomical coordinates as
353 described above. For the remainder of the analyses, the DH was then divided into 5 bins along the ML or
354 SD axes and the raw unnormalized count of Fos positive cells per bin was used.

355 **Computational modelling:** To adapt the Koulakov model (*8*, *49*, *50*) to the DH ST map, we added
356 parameters governing the strength of Ten3/Lphn2 repulsion/attraction since the original model assumed all
357 repulsive/attractive interactions to be of equal strength which may not hold in our case. We also reasoned
358 that it was possible for activity-dependant refinement to be disrupted in our cKOs, either due to the synaptic

359 roles of Teneurins and Latrophilins (*70*), or as a secondary circuit-level consequence of ST miswiring,
360 which might then further contribute to the observed ML distribution shifts. We thus incorporated into our
361 model the ability for cKOs to affect activity-dependent refinement and added additional parameters to
362 govern how this interaction occurs, if at all. These parameters govern how much the effect of activity-
363 dependent refinement should be dampened in each cell based on the decrease in Ten3 or Lphn2 in that cell
364 compared to the amount it would express under wild-type conditions using the following formula:

365 $$f(x) = 1 - a \cdot \frac{x^{1/b}}{x^{1/b} + 1}$$

366 Where x is the absolute decrease in expression compared to wild-type conditions for that cell. For a
367 complete list of model parameters and their description see Table S1. The Koulakov model itself has been
368 described in detail previously (*8*, *51*). Briefly, the model stochastically adds or removes connections to
369 attempt to minimize a global energy value $E = E_{chem} + E_{act} + E_{comp}$ that contains three components:
370 chemoaffinity energy (E_{chem}), activity energy (E_{act}), and competition energy (E_{comp}) where the
371 probability of adding or removing a connection proportional to the change in energy. E_{chem} is calculated
372 according to the following equation:

373 $$E_{chem} = a_{chem} \cdot \sum_{(A,D)\epsilon S_C} k_{tl} \cdot t(D) \cdot l(A) + k_{lt} \cdot l(D) \cdot t(A) - k_{tt} \cdot t(D) \cdot t(A)$$

374 With functions *t* and *l* describing the levels of Ten3 and Lphn2 in a given axon *A* or dendrite *D* and S_C
375 denoting the set of all connected pairs of axons and dendrites. Meanwhile E_{act} is calculated according to:

376 $$E_{act} = -\frac{\gamma}{2} \sum_{(A_1,D_1),(A_2,D_2)\epsilon S_C} e^{-dist(A_1,A_2)/b_{act}} \cdot e^{-dist(D_1,D_2)^2/2a_{act}^2}$$

377 and E_{comp} by:

378 $$E_{comp} = \sum_{A\epsilon S_A} -a_{comp} \cdot \sqrt[2]{n(A)} + b_{comp} \cdot n(A)^2 + \sum_{D\epsilon S_D} d_{comp} \cdot n(D)^2$$

Where n describes the number of synapses formed by a given axon or dendrite and S_A and S_D describing the sets of all axons and dendrites respectively. Parameter values for the Koulakov model (Table S1) were fit using ABC-SMC (*71*) using the PyABC package (version 0.12.16) (*72*). PyABC was run with a population size of 1000, and with maximum number of populations equal to 10, and epsilon values determined using the quantile epsilon method with parameters alpha equal to 0.1. From this, we obtained posterior distributions over the simulation parameters and a point estimate for the best model (Table S1).

Statistical Analysis: All statistical analyses were performed in R (version 4.0.5) and the specific statistical tests used are described in figure legends.

References:

1. R. W. Sperry, Chemoaffinity in the orderly growth of nerve fiber patterns and connections*. *Proceedings of the National Academy of Sciences* **50**, 703–710 (1963).

2. J. Walter, B. Kern-Veits, J. Huf, B. Stolze, F. Bonhoeffer, Recognition of position-specific properties of tectal cell membranes by retinal axons in vitro. *Development* **101**, 685–696 (1987).

3. H. T. Cline, M. Constantine-Paton, NMDA receptor antagonists disrupt the retinotectal topographic map. *Neuron* **3**, 413–426 (1989).

4. J. Frisén, P. A. Yates, T. McLaughlin, G. C. Friedman, D. D. M. O'Leary, M. Barbacid, Ephrin-A5 (AL-1/RAGS) Is Essential for Proper Retinal Axon Guidance and Topographic Mapping in the Mammalian Visual System. *Neuron* **20**, 235–243 (1998).

5. D. A. Feldheim, Y.-I. Kim, A. D. Bergemann, J. Frisén, M. Barbacid, J. G. Flanagan, Genetic Analysis of Ephrin-A2 and Ephrin-A5 Shows Their Requirement in Multiple Aspects of Retinocollicular Mapping. *Neuron* **25**, 563–574 (2000).

6. A. Brown, P. A. Yates, P. Burrola, D. Ortuño, A. Vaidya, T. M. Jessell, S. L. Pfaff, D. D. M. O'Leary, G. Lemke, Topographic Mapping from the Retina to the Midbrain Is Controlled by Relative but Not Absolute Levels of EphA Receptor Signaling. *Cell* **102**, 77–88 (2000).

7. T. Rashid, A. L. Upton, A. Blentic, T. Ciossek, B. Knöll, I. D. Thompson, U. Drescher, Opposing Gradients of Ephrin-As and EphA7 in the Superior Colliculus Are Essential for Topographic Mapping in the Mammalian Visual System. *Neuron* **47**, 57–69 (2005).

8. J. W. Triplett, C. Pfeiffenberger, J. Yamada, B. K. Stafford, N. T. Sweeney, A. M. Litke, A. Sher, A. A. Koulakov, D. A. Feldheim, Competition is a driving force in topographic mapping. *Proceedings of the National Academy of Sciences* **108**, 19060–19065 (2011).

9. G. Grant, J. Ygge, Somatotopic organization of the thoracic spinal nerve in the dorsal horn demonstrated with transganglionic degeneration. *Journal of Comparative Neurology* **202**, 357–364 (1981).

10. Y. Takahashi, T. Chiba, M. Kurokawa, Y. Aoki, Dermatomes and the central organization of dermatomes and body surface regions in the spinal cord dorsal horn in rats. *Journal of Comparative Neurology* **462**, 29–41 (2003).

11. K. Odagaki, H. Kameda, T. Hayashi, M. Sakurai, Mediolateral and dorsoventral projection patterns of cutaneous afferents within transverse planes of the mouse spinal dorsal horn. *Journal of Comparative Neurology* **527**, 972–984 (2019).

12. S. G. Nord, Somatotopic organization in the spinal trigeminal nucleus, the dorsal column nuclei and related structures in the rat. *Journal of Comparative Neurology* **130**, 343–356 (1967).

13. S. Maslany, D. P. Crockett, M. D. Egger, Somatotopic organization of the dorsal column nuclei in the rat: transganglionic labelling with B-HRP and WGA-HRP. *Brain Research* **564**, 56–65 (1991).

14. S. L. Florence, J. T. Wall, J. H. Kaas, Somatotopic organization of inputs from the hand to the spinal gray and cuneate nucleus of monkeys with observations on the cuneate nucleus of humans. *Journal of Comparative Neurology* **286**, 48–70 (1989).

15. J. T. Francis, S. Xu, J. K. Chapin, Proprioceptive and Cutaneous Representations in the Rat Ventral Posterolateral Thalamus. *Journal of Neurophysiology* **99**, 2291–2304 (2008).

16. R. R. Tasker, L. W. Organ, P. Hawrylyshyn, Sensory Organization of the Human Thalamus. *Applied Neurophysiology* **39**, 139–153 (1976).

17. W. Penfield, E. Boldrey, Somatic motor and sensory representation in the cerebral cortex of man as studied by electrical stimulation. *Brain* **60**, 389–443 (1937).

18. F. F. Ebner, J. H. Kaas, "Chapter 24 - Somatosensory System" in *The Rat Nervous System (Fourth Edition)*, G. Paxinos, Ed. (Academic Press, San Diego, 2015; https://www.sciencedirect.com/science/article/pii/B9780123742452000243), pp. 675–701.

19. B. Rexed, The cytoarchitectonic organization of the spinal cord in the cat. *Journal of Comparative Neurology* **96**, 415–495 (1952).

20. G. Gatto, S. Bourane, X. Ren, S. Di Costanzo, P. K. Fenton, P. Halder, R. P. Seal, M. D. Goulding, A Functional Topographic Map for Spinal Sensorimotor Reflexes. *Neuron* **109**, 91-104.e5 (2021).

21. W. D. Willis, R. E. Coggeshall, *Sensory Mechanisms of the Spinal Cord* (Springer US, Boston, MA, 1991; http://link.springer.com/10.1007/978-1-4899-0597-0).

22. A. Levinsson, H. Holmberg, J. Broman, M. Zhang, J. Schouenborg, Spinal Sensorimotor Transformation: Relation between Cutaneous Somatotopy and a Reflex Network. *J. Neurosci.* **22**, 8170–8182 (2002).

23. E. Bullitt, Somatotopy of spinal nociceptive processing. *Journal of Comparative Neurology* **312**, 279–290 (1991).

24. C. Molander, J. Hongpaisan, P. Shortland, Somatotopic redistribution of c-fos expressing neurons in the superficial dorsal horn after peripheral nerve injury. *Neuroscience* **84**, 241–253 (1998).

25. T. Sugimoto, H. Ichikawa, S. Mitani, A. Hitsu, N. Tadao, Changes in c-fos induction in dorsal horn neurons by hindpaw formalin stimulation following tibial neurotomy. *Brain Research* **642**, 348–354 (1994).

26. M. Tabata, R. Terayama, K. Maruhama, S. Iida, T. Sugimoto, Differential induction of c-Fos and phosphorylated ERK by a noxious stimulus after peripheral nerve injury. *International Journal of Neuroscience* **128**, 208–218 (2018).

27. C. Warwick, J. Salsovic, J. Hachisuka, K. M. Smith, T. D. Sheahan, H. Chen, J. Ibinson, H. R. Koerber, S. E. Ross, Cell type-specific calcium imaging of central sensitization in mouse dorsal horn. *Nat Commun* **13**, 5199 (2022).

28. K. Mirnics, H. R. Koerher, Prenatal development of rat primary afferent fibers: II. Central projections. *Journal of Comparative Neurology* **355**, 601–614 (1995).

29. A. S. F. Grünbaum, C. S. Sherrington, Observations on the physiology of the cerebral cortex of some of the higher apes. (Preliminary communication.). *Proceedings of the Royal Society of London* **69**, 206–209 (1901).

30. R. Hassler, "New Aspects of Brain Functions Revealed by Brain Diseases" in *Frontiers in Brain Research*, J. D. French, Ed. (Columbia University Press, 2019; http://www.degruyterbrill.com/document/doi/10.7312/fren91252-011/html), pp. 242–288.

31. E. M. Gordon, R. J. Chauvin, A. N. Van, A. Rajesh, A. Nielsen, D. J. Newbold, C. J. Lynch, N. A. Seider, S. R. Krimmel, K. M. Scheidter, J. Monk, R. L. Miller, A. Metoki, D. F. Montez, A. Zheng, I. Elbau, T. Madison, T. Nishino, M. J. Myers, S. Kaplan, C. Badke D'Andrea, D. V. Demeter, M. Feigelis, J. S. B. Ramirez, T. Xu, D. M. Barch, C. D. Smyser, C. E. Rogers, J. Zimmermann, K. N. Botteron, J. R. Pruett, J. T. Willie, P. Brunner, J. S. Shimony, B. P. Kay, S. Marek, S. A. Norris, C. Gratton, C. M. Sylvester, J. D. Power, C. Liston, D. J. Greene, J. L. Roland, S. E. Petersen, M. E. Raichle, T. O. Laumann, D. A. Fair, N. U. F. Dosenbach, A somato-cognitive action network alternates with effector regions in motor cortex. *Nature* **617**, 351–359 (2023).

32. B. Mendelson, Chronic embryonic MK-801 exposure disrupts the somatotopic organization of cutaneous nerve projections in the chick spinal cord. *Developmental Brain Research* **82**, 152–166 (1994).

33. S. Beggs, C. Torsney, L. J. Drew, M. Fitzgerald, The postnatal reorganization of primary afferent input and dorsal horn cell receptive fields in the rat spinal cord is an activity-dependent process. *European Journal of Neuroscience* **16**, 1249–1258 (2002).

34. M. Granmo, P. Petersson, J. Schouenborg, Action-Based Body Maps in the Spinal Cord Emerge from a Transitory Floating Organization. *J. Neurosci.* **28**, 5494–5503 (2008).

35. C. L. Smith, The development and postnatal organization of primary afferent projections to the rat thoracic spinal cord. *Journal of Comparative Neurology* **220**, 29–43 (1983).

36. M. Fitzgerald, Prenatal growth of fine-diameter primary afferents into the rat spinal cord: A transganglionic tracer study. *Journal of Comparative Neurology* **261**, 98–104 (1987).

37. I. Silos-Santiago, B. Jeng, W. D. Snider, Sensory afferents show appropriate somatotopy at the earliest stage of projection to dorsal horn: *NeuroReport* **6**, 861–865 (1995).

38. M. J. Arcaro, P. F. Schade, M. S. Livingstone, Body map proto-organization in newborn macaques. *Proceedings of the National Academy of Sciences* **116**, 24861–24871 (2019).

39. D. S. Berns, L. A. DeNardo, D. T. Pederick, L. Luo, Teneurin-3 controls topographic circuit assembly in the hippocampus. *Nature* **554**, 328–333 (2018).

40. D. T. Pederick, J. H. Lui, E. C. Gingrich, C. Xu, M. J. Wagner, Y. Liu, Z. He, S. R. Quake, L. Luo, Reciprocal repulsions instruct the precise assembly of parallel hippocampal networks. *Science* (2021).

41. E. C. Gringrich, D. T. Pederick, Y. Zhang, L. Luo, Ten3–Lphn2-mediated target selection across the extended hippocampal network demonstrates a repeated strategy for circuit assembly. *bioRxiv* (2025).

42. S. Ozaki, W. D. Snider, Initial trajectories of sensory axons toward laminar targets in the developing mouse spinal cord. *Journal of Comparative Neurology* **380**, 215–229 (1997).

43. H. Hasegawa, S. Abbott, B.-X. Han, Y. Qi, F. Wang, Analyzing Somatosensory Axon Projections with the Sensory Neuron-Specific Advillin Gene. *J. Neurosci.* **27**, 14404–14414 (2007).

44. G. R. Anderson, S. Maxeiner, R. Sando, T. Tsetsenis, R. C. Malenka, T. C. Südhof, Postsynaptic adhesion GPCR latrophilin-2 mediates target recognition in entorhinal-hippocampal synapse assembly. *Journal of Cell Biology* **216**, 3831–3846 (2017).

45. C. Molander, G. Grant, Cutaneous projections from the rat hindlimb foot to the substantia gelatinosa of the spinal cord studied by transganglionic transport of WGA-HRP conjugate. *Journal of Comparative Neurology* **237**, 476–484 (1985).

46. A. Prats-Galino, A. Puigdellívol-sánchez, D. Ruano-Gil, C. Molander, Representations of hindlimb digits in rat dorsal root ganglia. *Journal of Comparative Neurology* **408**, 137–145 (1999).

47. S. Maslany, D. P. Crockett, M. David Egger, Organization of cutaneous primary afferent fibers projecting to the dorsal horn in the rat: WGA-HRP versus B-HRP. *Brain Research* **569**, 123–135 (1992).

48. J. E. Swett, C. J. Woolf, The somatotopic organization of primary afferent terminals in the superficial laminae of the dorsal horn of the rat spinal cord. *Journal of Comparative Neurology* **231**, 66–77 (1985).

49. A. A. Koulakov, D. N. Tsigankov, A stochastic model for retinocollicular map development. *BMC Neurosci* **5**, 30 (2004).

50. D. N. Tsigankov, A. A. Koulakov, A unifying model for activity-dependent and activity-independent mechanisms predicts complete structure of topographic maps in ephrin-A deficient mice. *J Comput Neurosci* **21**, 101–114 (2006).

51. J. J. J. Hjorth, D. C. Sterratt, C. S. Cutts, D. J. Willshaw, S. J. Eglen, Quantitative assessment of computational models for retinotopic map formation. *Developmental Neurobiology* **75**, 641–666 (2015).

52. M. Fitzgerald, The sprouting of saphenous nerve terminals in the spinal cord following early postnatal sciatic nerve section in the rat. *Journal of Comparative Neurology* **240**, 407–413 (1985).

53. M. Fitzgerald, C. J. Woolf, P. Shortland, Collateral sprouting of the central terminals of cutaneous primary afferent neurons in the rat spinal cord: Pattern, morphology, and influence of targets. *Journal of Comparative Neurology* **300**, 370–385 (1990).

54. C. A. Leamey, S. Merlin, P. Lattouf, A. Sawatari, X. Zhou, N. Demel, K. A. Glendining, T. Oohashi, M. Sur, R. Fässler, Ten_m3 Regulates Eye-Specific Patterning in the Mammalian Visual Pathway and Is Required for Binocular Vision. *PLOS Biology* **5**, e241 (2007).

55. P. Suetterlin, U. Drescher, Target-Independent EphrinA/EphA-Mediated Axon-Axon Repulsion as a Novel Element in Retinocollicular Mapping. *Neuron* **84**, 740–752 (2014).

56. P. Vanderhaeghen, Q. Lu, N. Prakash, J. Frisén, C. A. Walsh, R. D. Frostig, J. G. Flanagan, A mapping label required for normal scale of body representation in the cortex. *Nat Neurosci* **3**, 358–365 (2000).

57. A. Dufour, J. Seibt, L. Passante, V. Depaepe, T. Ciossek, J. Frisén, K. Kullander, J. G. Flanagan, F. Polleux, P. Vanderhaeghen, Area Specificity and Topography of Thalamocortical Projections Are Controlled by ephrin/Eph Genes. *Neuron* **39**, 453–465 (2003).

58. Ur. Chon, D. T. Pederick, J. T. Song, Y. Zhang, Rana, L. Luo, Inverse expression of Ten3 and Lphn2 across the developing mouse brain reveals a global strategy for circuit assembly. *bioRxiv* (2025).

59. R. Melzack, K. Casey, Sensory, motivational, and central control determinants of pain. Kenshalo DR, editor. The skin senses: proceedings. Springfield (Illinois): Charles C. *Thomas*, 423–443 (1968).

60. M. A. Sieber, R. Storm, M. Martinez-de-la-Torre, T. Müller, H. Wende, K. Reuter, E. Vasyutina, C. Birchmeier, Lbx1 Acts as a Selector Gene in the Fate Determination of Somatosensory and Viscerosensory Relay Neurons in the Hindbrain. *J. Neurosci.* **27**, 4902–4909 (2007).

61. T. Pietri, O. Eder, M. Blanche, J. P. Thiery, S. Dufour, The human tissue plasminogen activator-Cre mouse: a new tool for targeting specifically neural crest cells and their derivatives in vivo. *Developmental Biology* **259**, 176–187 (2003).

62. H. C. Lai, R. P. Seal, J. E. Johnson, Making sense out of spinal cord somatosensory development. *Development* **143**, 3434–3448 (2016).

63. T. Müller, H. Brohmann, A. Pierani, P. A. Heppenstall, G. R. Lewin, T. M. Jessell, C. Birchmeier, The Homeodomain Factor Lbx1 Distinguishes Two Major Programs of Neuronal Differentiation in the Dorsal Spinal Cord. *Neuron* **34**, 551–562 (2002).

64. S. Paixão, A. Balijepalli, N. Serradj, J. Niu, W. Luo, J. H. Martin, R. Klein, EphrinB3/EphA4-Mediated Guidance of Ascending and Descending Spinal Tracts. *Neuron* **80**, 1407–1420 (2013).

65. S. Hunskaar, K. Hole, The formalin test in mice: dissociation between inflammatory and non-inflammatory pain. *Pain* **30**, 103–114 (1987).

66. J. S. Mogil, S. G. Wilson, K. Bon, S. Eun Lee, K. Chung, P. Raber, J. O. Pieper, H. S. Hain, J. K. Belknap, L. Hubert, G. I. Elmer, J. Mo Chung, M. Devor, Heritability of nociception I: Responses of 11 inbred mouse strains on 12 measures of nociception. *Pain* **80**, 67–82 (1999).

67. R. B. Roome, F. B. Bourojeni, B. Mona, S. Rastegar-Pouyani, R. Blain, A. Dumouchel, C. Salesse, W. S. Thompson, M. Brookbank, Y. Gitton, L. Tessarollo, M. Goulding, J. E. Johnson, M. Kmita, A. Chédotal, A. Kania, Phox2a Defines a Developmental Origin of the Anterolateral System in Mice and Humans. *Cell Reports* **33**, 108425 (2020).

68. P. Bankhead, M. B. Loughrey, J. A. Fernández, Y. Dombrowski, D. G. McArt, P. D. Dunne, S. McQuaid, R. T. Gray, L. J. Murray, H. G. Coleman, J. A. James, M. Salto-Tellez, P. W. Hamilton, QuPath: Open source software for digital pathology image analysis. *Sci Rep* **7**, 16878 (2017).

69. U. Schmidt, M. Weigert, C. Broaddus, G. Myers, "Cell Detection with Star-Convex Polygons" in *Medical Image Computing and Computer Assisted Intervention – MICCAI 2018*, A. F. Frangi, J. A. Schnabel, C. Davatzikos, C. Alberola-López, G. Fichtinger, Eds. (Springer International Publishing, Cham, 2018)*Lecture Notes in Computer Science*, pp. 265–273.

70. T. C. Südhof, Signaling by latrophilin adhesion-GPCRs in synapse assembly. *Neuroscience*, doi: 10.1016/j.neuroscience.2025.03.041 (2025).

71. S. A. Sisson, Y. Fan, M. Beaumont, *Handbook of Approximate Bayesian Computation* (CRC Press, 2018).

72. Y. Schälte, E. Klinger, E. Alamoudi, J. Hasenauer, pyABC: Efficient and robust easy-to-use approximate Bayesian computation. *Journal of Open Source Software* **7**, 4304 (2022).

590 **Fig. 1. Complementary expression of *Ten3* and *Lphn2* in the DH and DRG.** (**A**) RNAscope for *Ten3*
591 and *Lphn2* mRNA in the lumbosacral dorsal horn at e14.5 (left). Quantification of RNAscope puncta and
592 fluorescence intensity (right). (**B**) Immunostaining for Ten3 and Lphn2 (anti-GFP antibody) in the lumbar
593 dorsal horn and adjacent dorsal root entry zone (DREZ) of *Lphn2-mVenus* knock-in mice at e14.5 (left).
594 Quantification of fluorescence intensity in the DH (right) (**C**) RNAscope for *Ten3* and *Lphn2* in lumbar
595 dorsal root ganglia at e14.5 (left) and quantification of RNAscope puncta (right). (**D**) Hypothesized
596 interactions governing DH somatotopic map formation based on the expression and previously described
597 roles of Ten3 and Lphn2. All data shown as mean ± SEM. Scale bars in A, B = 100 μm, C = 50 μm. Axis
598 labels in this and subsequent figures: M, medial; L, ventral; D, dorsal; V, ventral

599

600 **Fig. 2. Altered somatotopy of distal sensory afferents in Ten3 and Lphn2 cKOs.** (**A** and **D**) Schematic
601 of lost and preserved interactions in (A) Ten3$^{\Delta DH}$ cKOs and (D) Lphn2$^{\Delta DRG}$ cKOs (top) and the observed
602 shift in the ST distribution of afferents in the cKOs (bottom, filled lines) compared to controls (bottom,
603 dotted lines). (**B** and **E**) Representative images of CTB and WGA labeled afferents in (B) Ten3$^{\Delta DH}$ cKOs
604 and (E) Lphn2$^{\Delta DRG}$ cKOs compared to controls. (**C** and **F**) Quantification of the distribution of CTB and
605 WGA signal across the ML axis of the DH in cKOs and control littermates. All data shown as mean ±
606 SEM. Two-way mixed ANOVA was performed and genotype x bin interaction terms are reported. ***P ≤
607 0.001; **P ≤ 0.01; *P ≤ 0.05. Scale bars = 100 μm.

608

609 **Fig. 3. Altered somatotopy of proximal sensory afferents in Ten3 and Lphn2 cKOs.** (**A**, **D** and **G**)
610 Schematic of lost and preserved interactions in (A) Ten3$^{\Delta DH}$ cKOs, (D) Lphn2$^{\Delta DH}$ cKOs, and (G)
611 Ten3$^{\Delta DRG}$ cKOs (top) and the observed shift in the ST distribution of afferents in the cKOs (bottom, filled
612 lines) compared to controls (bottom, dotted lines). (**B**, **E** and **H**) Representative images of CTB and WGA
613 labeled afferents in (B) Ten3$^{\Delta DH}$ cKOs (insets show more medially located CTB/WGA in cKOs), (E)
614 Lphn2$^{\Delta DH}$ cKOs, and (H) Ten3$^{\Delta DRG}$ cKOs compared to controls. (**C**, **F** and **I**) Quantification of the
615 distribution of CTB and WGA signal across the ML axis of the DH in cKOs and control littermates. All
616 data shown as mean ± SEM. Two-way mixed ANOVA was performed and genotype x bin interaction
617 terms are reported. ***P ≤ 0.001; **P ≤ 0.01; *P ≤ 0.05. Scale bars = 100 μm.

618

619 **Fig. 4. Computational modelling of DH somatotopic map formation.** (**A**) Simplified schematic of
620 model parameters and ABC-SMC procedure. (**B**) Correct distal → medial and proximal → lateral
621 mapping from one representative simulation under wild-type conditions. Simulated ML density of
622 terminal zones in the DH from 10 DRG axons selected across the PD axis. (**C**) Observed and simulated
623 tracer injections for controls and cKOs across all genotype/injection site combinations examined. Average
624 distributions of each condition are shown. Simulated distribution taken from the average of 10
625 independent simulations.

626

627 **Fig. 5. Altered ST of neural activity and behavioral responses induced by a noxious stimulus in**
628 **Ten3$^{\Delta DH}$ cKOs.** (**A**) Representative images of immunostaining for Fos in the DH induced by formalin
629 injection to the hindpaw of Ten3$^{\Delta DH}$ cKOs and contols. (**B-D**) Quantification of Fos positive cells in
630 Ten3$^{\Delta DH}$ cKO mice and control littermates. (B) Distribution of Fos positive cells across the ML axis of the
631 DH. Two-way mixed ANOVA test was performed and genotype x bin interaction term is reported along
632 with Benjamini-Yekutieli corrected post-hoc p-values for individual bin comparisons. (C) 2D kernel
633 density plots showing their distribution of Fos positive cells in the DH. Hotelling T^2 p-value 0.03. (D)
634 Average ML position of Fos cells. Welch's t-test was performed. (**E**) Quantification of nocifensive licking
635 behavior in response to formalin injection to the hindpaw near the digits, depicted as a percent of total

linking time per limb region. Two-way mixed ANOVA was performed and genotype x location interaction term is reported. Post-hoc Mann-Whitney tests were performed for each limb location. All data shown as mean ± SEM. ***P ≤ 0.001; **P ≤ 0.01; *P ≤ 0.05. Scale bars = 100 μm.

Fig. S1. Additional characterization of Ten3 and Lphn2 expression. (**A**) Dual RNAscope/Immunostaining for *Ten3* and *Lphn2* with DRG neuron subtype markers TrkA (left), TrkB (middle), and TrkC (right) in e14.5 DRG. (**B**) RNAscope for *Ten3* and *Lphn2* in e14.5 DRG cross sections (left) and quantification of puncta counts and fluorescence intensity (right) showing no spatial bias for either across the DV or ML axes. Insets show DRG neurons with high *Lphn2* (′), a mix of *Lphn2* and *Ten3* (″), and high *Ten3* (‴). (**C**) Quantification of RNAscope puncta in (B) for *Lphn2* in *Ten3*-low compared to *Ten3*-high cells and or *Ten3* in *Lphn2*-low compared to *Lphn2*-high cells. Counts per cell were averaged such that each point corresponds to one embryo. High cells were defined as the top 90% and low cells were defined as the bottom 10% of cells expressing each respective gene after filtering out cells that do not express either. (**D**) Related to Fig. 1B, quantification of fluorescence intensity of immunostaining for Ten3 and Lphn2 (anti-GFP antibody) in the white matter adjacent to the DH of Lphn2-mVenus knock-in mice at e14.5. Shown as fluorescence intensity normalized per image (left) or as a proportion of total fluorescence intensity at each ML position (right). (**E**) RNAscope for *Ten3* and *Lphn2* in the e16.5 ventrobasal (VB) thalamus aligning with the proximal to distal somatotopic organization (dorsolateral to ventromedial VB). (**F**) RNAscope for *TENM3* and *ADGRL2* (human orthologues of *Ten3* and *Lphn2*) in the human gestational week (GW) 20 DH. All data shown as mean ± SEM. A paired t-test was performed in (C). ***P ≤ 0.001; **P ≤ 0.01; *P ≤ 0.05. Scale bars in (A) = 25 μm, in (B, E and F) = 100 μm.

Fig. S2. Ten3 and Lphn2 guide DRG axons *in-vitro*. (**A**) Explants of e15.5 lumbar DRGs labelled with anti-βIII-tubulin antibody grown on stripes of: FC (black), FC (red, left), Lphn2-lectin domain (Lphn2-Lec, red, middle), or Lphn2 non-Teneurin-binding mutants (Lphn2-Lec^{LT}, red, right) proteins. Red stripes are also marked by white arrowheads. (**B**) Quantification of βIII-tubulin on red stripes as a percentage of the total βIII-tubulin signal. While there is no preference for red or black stripes in either FC/FC or FC/Lphn2-Lec^{LT} controls, there are significantly fewer βIII-tubulin labelled axons on the red Lphn2-Lec stripes. (**C**) Explants of e15.5 lumbar DRGs labelled with anti-βIII-tubulin antibody grown on stripes of: FC (black), FC (red, left), or Ten3 (red, right) proteins. Red stripes are also marked by white arrowheads. (**D**) Quantification of βIII-tubulin on red stripes as a percentage of the total βIII-tubulin signal. While there is no preference for red or black stripes in FC/FC controls, there are significantly fewer βIII-tubulin labelled axons on the red Ten3 stripes. ***P ≤ 0.001; **P ≤ 0.01; *P ≤ 0.05. Scale bars = 200 μm.

Fig. S3. Additional characterization of distal sensory afferents in Ten3 and Lphn2 cKOs. (**A**) Validation of cre lines used in this study showing cre-driven tdTomato expression in the DH and DRG at E11.5 and E16.5 (**B**) A representative example showing mapping of x and y axes to anatomically-relevant axes used in quantifications in this study to account for DH curvature. (**C** and **H**) ML distribution of WGA (left) and CTB (right) in (C) Ten3$^{\Delta DH}$ cKOs and (H) Lphn2$^{\Delta DRG}$ cKOs compared to littermate controls. (**D** and **I**) Average Pearson correlation coefficient per animal between WGA and CTB signal across the ML axis of the DH in (D) Ten3$^{\Delta DH}$ cKOs and (I) Lphn2$^{\Delta DRG}$ cKOs compared to littermate controls. (**E**, **F**, **J** and **K**) SD distribution of CTB and WGA signal in controls (E and J) and cKOs (F and K) showing SD separation of afferents labeled by the two tracers. (**G** and **L**) SD distribution of WGA (left) and CTB (right) between cKOs and control littermates showing no shift along this axis. All data shown as mean ± SEM. Welch's t-test was performed in (D) and (I), in all others two-way mixed ANOVA was performed and genotype x bin interaction term is reported. ***P ≤ 0.001; **P ≤ 0.01; *P ≤ 0.05. Scale bars = 100 μm.

Fig. S4. Additional characterization of proximal sensory afferents in Ten3 and Lphn2 cKOs. (**A**, **F** and **K**) ML distribution of WGA (left) and CTB (right) in (A) Ten3$^{\Delta DH}$ cKOs, (F) Lphn2$^{\Delta DH}$ cKOs, and (K) Ten3$^{\Delta DRG}$ cKOs compared to littermate controls. (**B**, **G** and **L**) Average Pearson correlation coefficient per animal between WGA and CTB signal across the ML axis of the DH in (B) Ten3$^{\Delta DH}$ cKOs, (G) Lphn2$^{\Delta DH}$ cKOs, and (L) Ten3$^{\Delta DRG}$ cKOs compared to littermate controls. (**C**, **D**, **H**, **I**, **M** and **N**) SD distribution of CTB and WGA signal in controls (C, H, and M) and cKOs (D, I, and N) showing SD separation of afferents labeled by the two tracers. (**E**, **J** and **O**) SD distribution of WGA (left) and CTB (right) between cKOs and control littermates. All data shown as mean ± SEM. Welch's t-test was performed in (B), (G) and (L), in all others two-way mixed ANOVA was performed and genotype x bin interaction term is reported. ***$P \leq 0.001$; **$P \leq 0.01$; *$P \leq 0.05$.

Fig. S5. Further evaluation of computational model performance. (**A**) PD origin of DRG axons compared to the position of their ML terminal zones showing correct distal → medial and proximal → lateral mapping from one representative simulation under wild-type conditions. (**B** and **C**) Simulated nerve cut experiment from one representative simulation under wild-type conditions showing expansion of remaining axons along the entire ML extent of the DH. (B) PD origin of DRG axons compared to the position of their ML terminal zones. (C) Simulated ML density of terminal zones in the DH from 10 DRG axons selected across the PD axis.

Fig. S6. Additional characterization of neural activity and somatosensory behavioral responses in Ten3 mutants. (**A** and **B**) Related to Fig. 5, quantification of Fos+ cells in the contralateral and ipsilateral DH relative to the side of the formalin injection in (A) controls and (B) cKOs. (**C** and **D**) Quantification of Fos+ cells in cKOs compared to littermate controls in the (C) contralateral and (D) ipsilateral DH relative to the site of injection. (**E**) SD distribution of Fos+ cells in cKOs compared to littermate controls in the ipsilateral DH. (**F-H**) Quantification of nocifensive licking behavior in Ten3 global KOs compared to control littermates in response to formalin injection to the hindpaw near the digits. (F) The percent of total licking time per limb region. (G) Licking time in seconds per limb region. (H) Total licking time. (**I**) Latency to remove adhesive tape from the hindpaw in KOs and control littermates. (**J**) Number of attempts to remove adhesive tape from the hindpaw in KOs and littermate controls. (**L-N**) Same as in panels (F), and (H-J) respectively, except performed in Ten3$^{\Delta DH}$ cKOs and control littermates. All data shown as mean ± SEM. Welch's t-test was performed in (A-D) and Mann-Whitney tests were performed in (H-J) and (K-N). In (F), (G) and (L) a two-way mixed ANOVA was performed, genotype x bin interaction term is reported, and post-hoc Mann-Whitney tests were performed for each limb location. ***$P \leq 0.001$; **$P \leq 0.01$; *$P \leq 0.05$. Scale bars = 100 μm

Figure 1

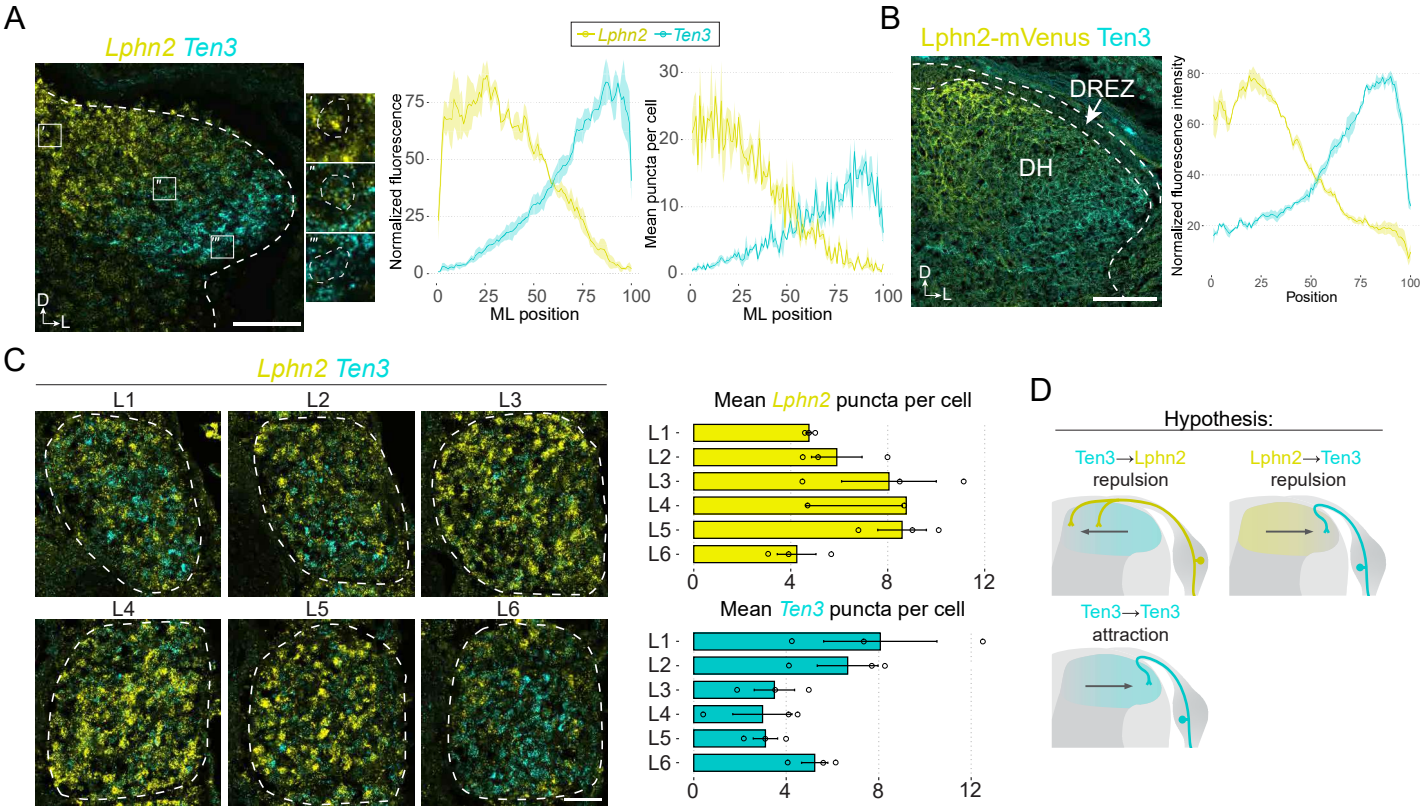
A
Lphn2 Ten3
D
L
Lphn2
Ten3
Normalized fluorescence
ML position
Mean puncta per cell
ML position
B
Lphn2-mVenus Ten3
DREZ
DH
D
L
Normalized fluorescence intensity
Position
C
Lphn2 Ten3
L1
L2
L3
L4
L5
L6
Mean Lphn2 puncta per cell
Mean Ten3 puncta per cell
D
Hypothesis:
Ten3→Lphn2
repulsion
Lphn2→Ten3
repulsion
Ten3→Ten3
attraction

Figure 2

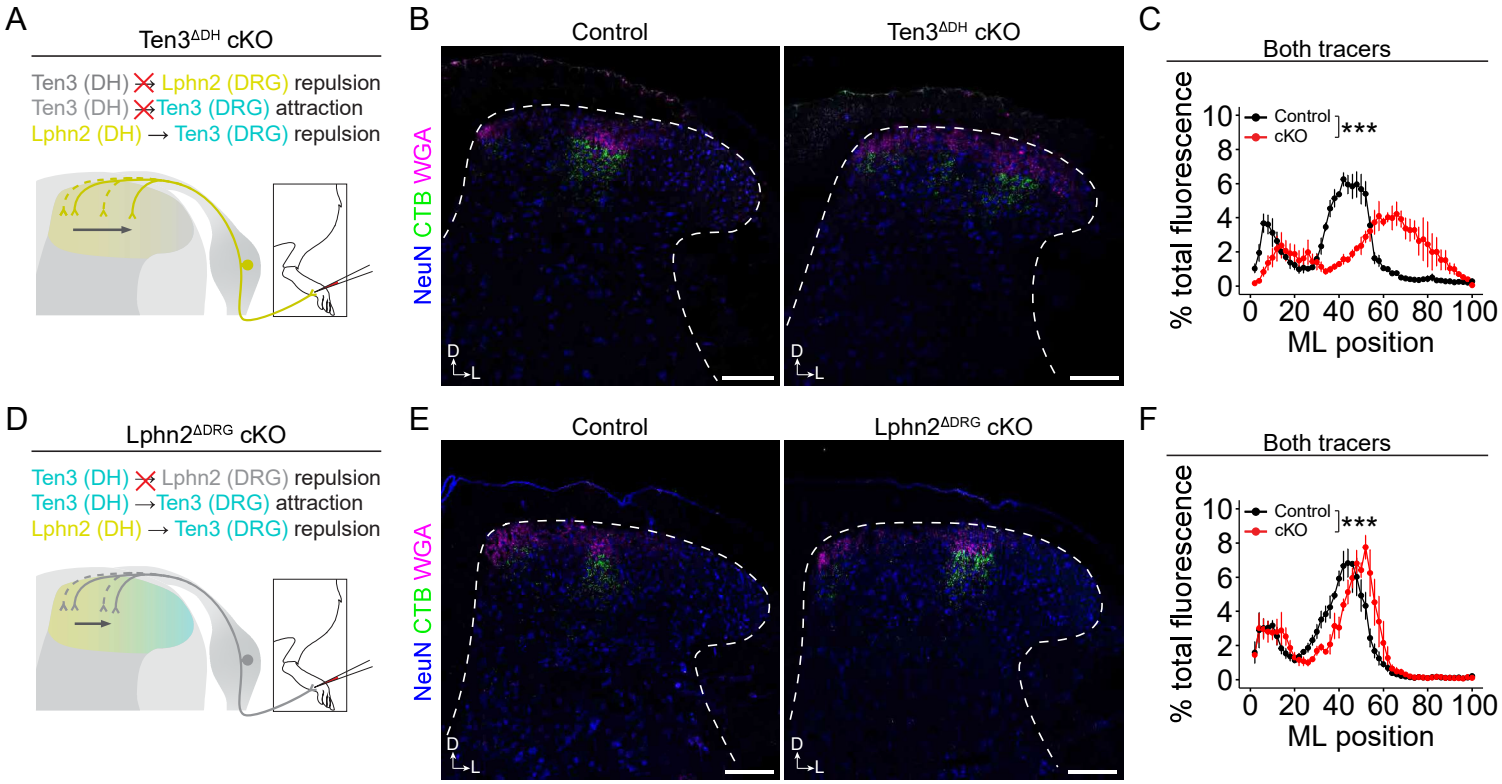
A
Ten3ΔDH cKO
Ten3 (DH) ⤫ Lphn2 (DRG) repulsion
Ten3 (DH) ⤫ Ten3 (DRG) attraction
Lphn2 (DH) → Ten3 (DRG) repulsion
B
Control
Ten3ΔDH cKO
NeuN CTB WGA
D
L
C
Both tracers
Control
cKO
***
% total fluorescence
ML position
0 20 40 60 80 100
0 2 4 6 8 10
D
Lphn2ΔDRG cKO
Ten3 (DH) ⤫ Lphn2 (DRG) repulsion
Ten3 (DH) → Ten3 (DRG) attraction
Lphn2 (DH) → Ten3 (DRG) repulsion
E
Control
Lphn2ΔDRG cKO
NeuN CTB WGA
D
L
F
Both tracers
Control
cKO
***
% total fluorescence
ML position
0 20 40 60 80 100
0 2 4 6 8 10

Figure 3

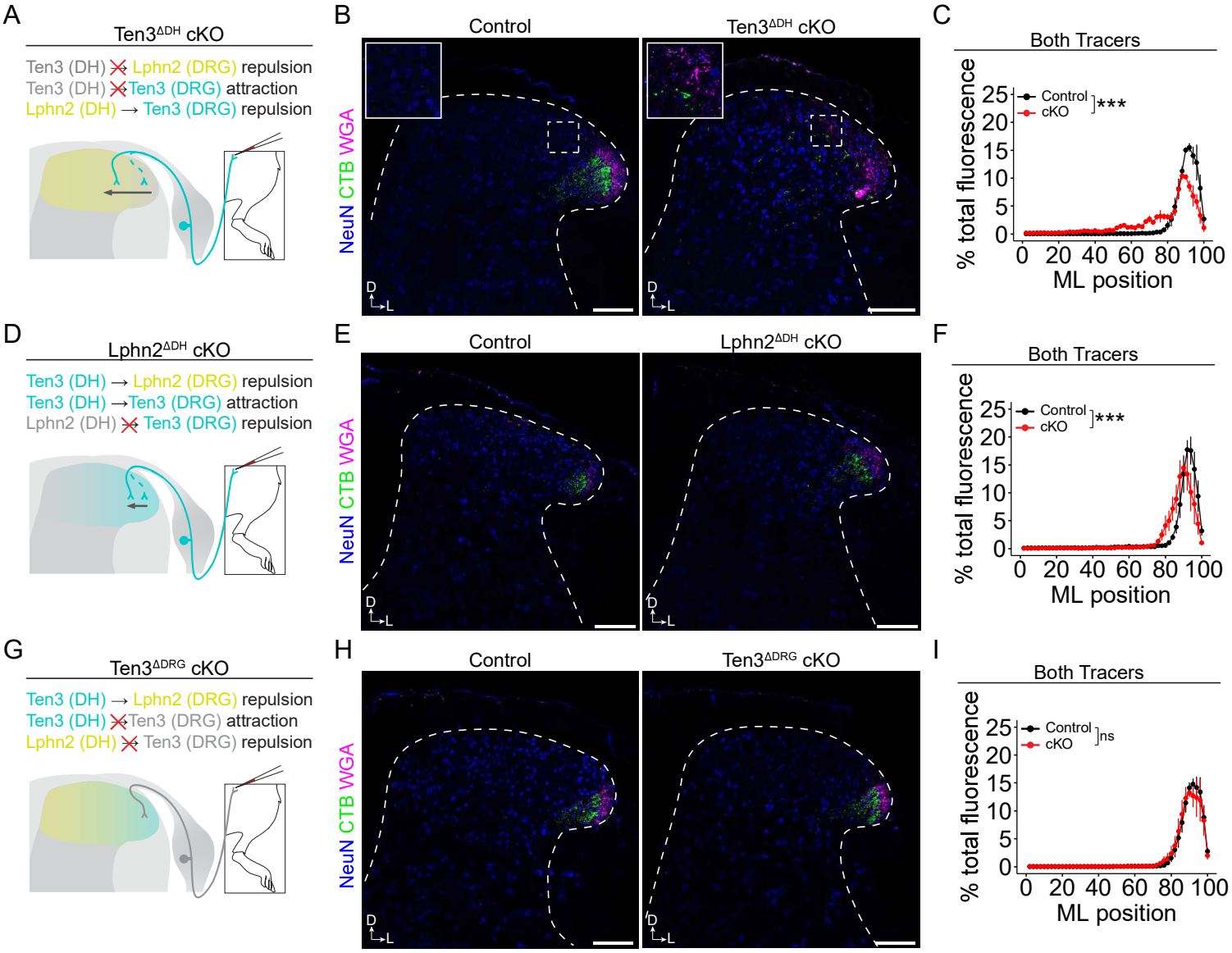
A
Ten3ΔDH cKO
Ten3 (DH) ⤫ Lphn2 (DRG) repulsion
Ten3 (DH) ⤫ Ten3 (DRG) attraction
Lphn2 (DH) → Ten3 (DRG) repulsion
B
Control
Ten3ΔDH cKO
NeuN CTB WGA
D
L
C
Both Tracers
Control
cKO
***
% total fluorescence
ML position
D
Lphn2ΔDH cKO
Ten3 (DH) → Lphn2 (DRG) repulsion
Ten3 (DH) → Ten3 (DRG) attraction
Lphn2 (DH) ⤫ Ten3 (DRG) repulsion
E
Control
Lphn2ΔDH cKO
F
Both Tracers
G
Ten3ΔDRG cKO
Ten3 (DH) → Lphn2 (DRG) repulsion
Ten3 (DH) ⤫ Ten3 (DRG) attraction
Lphn2 (DH) ⤫ Ten3 (DRG) repulsion
H
Control
Ten3ΔDRG cKO
I
Both Tracers
ns

Figure 4

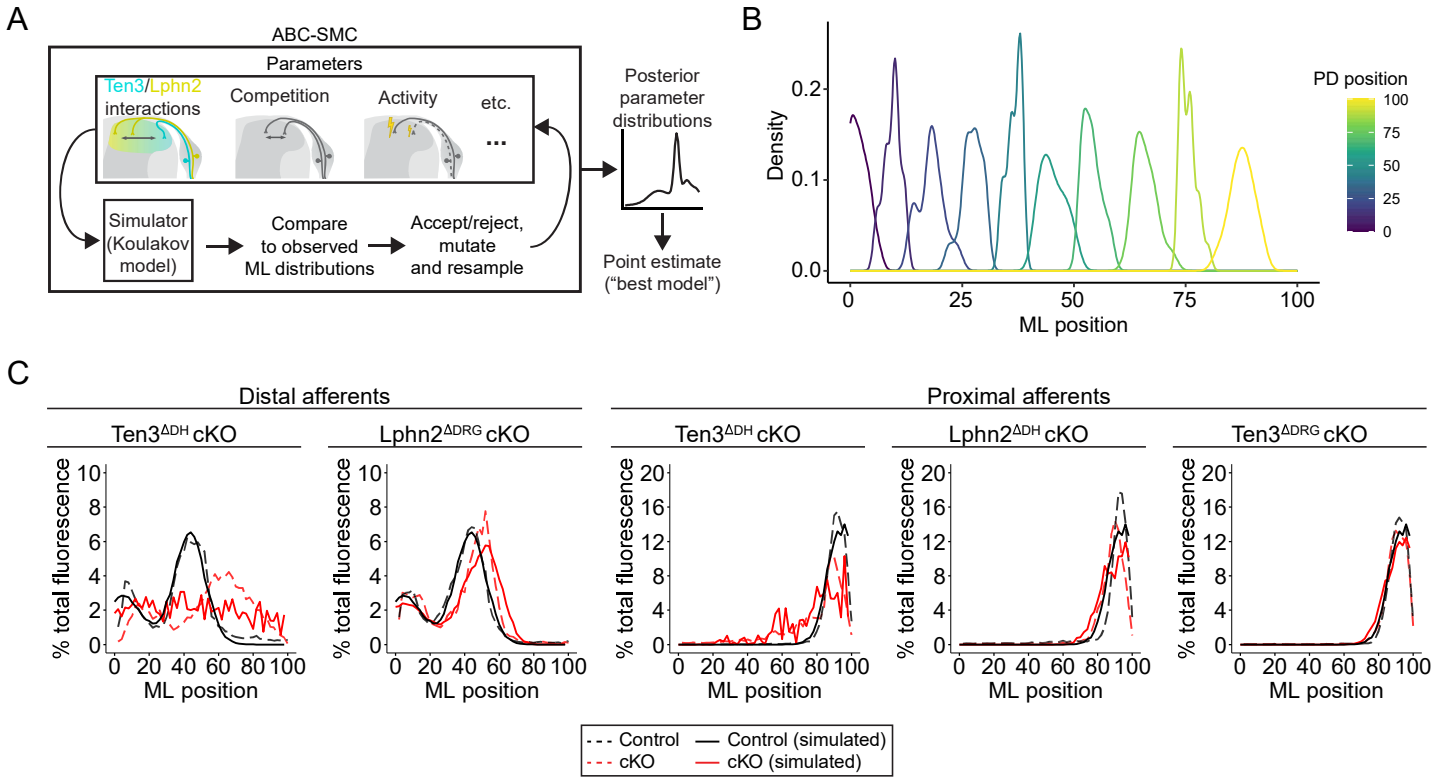
A
ABC-SMC
Parameters
Ten3/Lphn2 interactions
Competition
Activity
etc.
...
Simulator (Koulakov model)
Compare to observed ML distributions
Accept/reject, mutate and resample
Posterior parameter distributions
Point estimate ("best model")
B
Density
ML position
PD position
C
Distal afferents
Proximal afferents
Ten3ΔDH cKO
Lphn2ΔDRG cKO
Lphn2ΔDH cKO
Ten3ΔDRG cKO
% total fluorescence
ML position
Control
cKO
Control (simulated)
cKO (simulated)

Figure 5

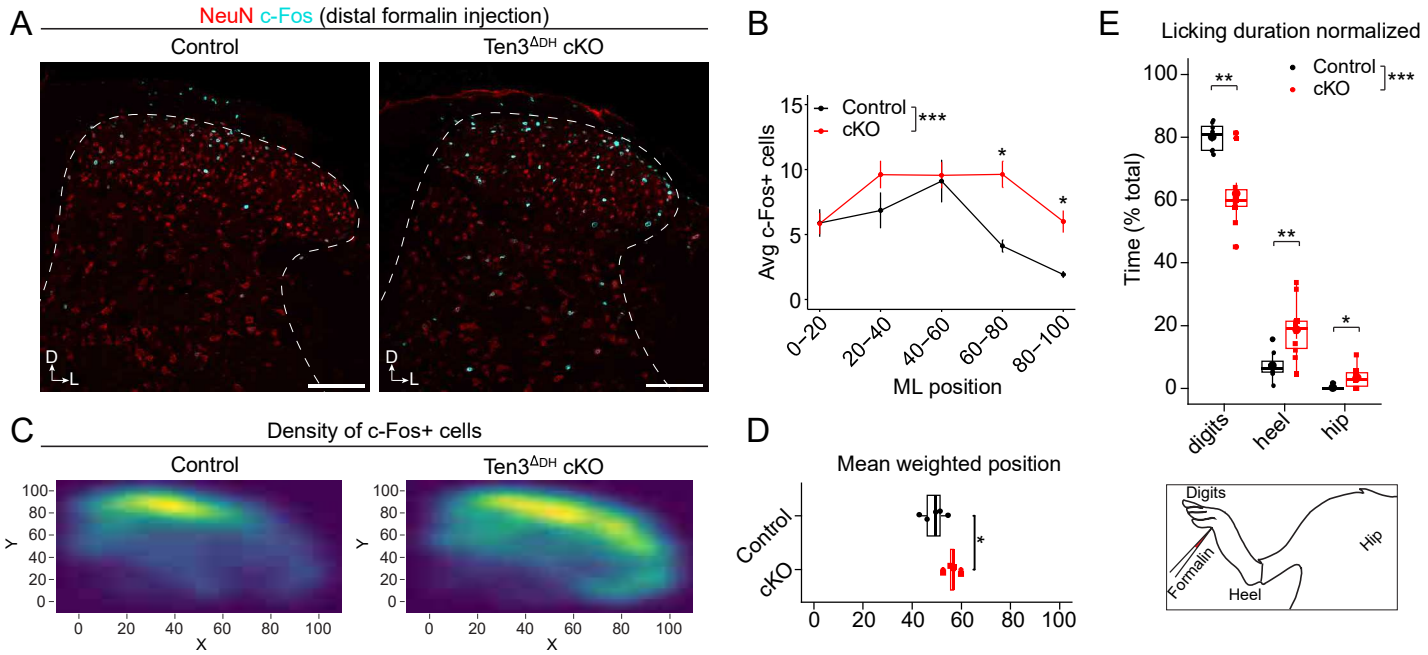
A
NeuN c-Fos (distal formalin injection)
Control
Ten3ΔDH cKO
D
L
B
Control
cKO
***
Avg c-Fos+ cells
ML position
0–20
20–40
40–60
60–80
80–100
C
Density of c-Fos+ cells
Control
Ten3ΔDH cKO
Y
X
D
Mean weighted position
Control
cKO
E
Licking duration normalized
Control
cKO
Time (% total)
digits
heel
hip
Digits
Hip
Formalin
Heel

Figure S1

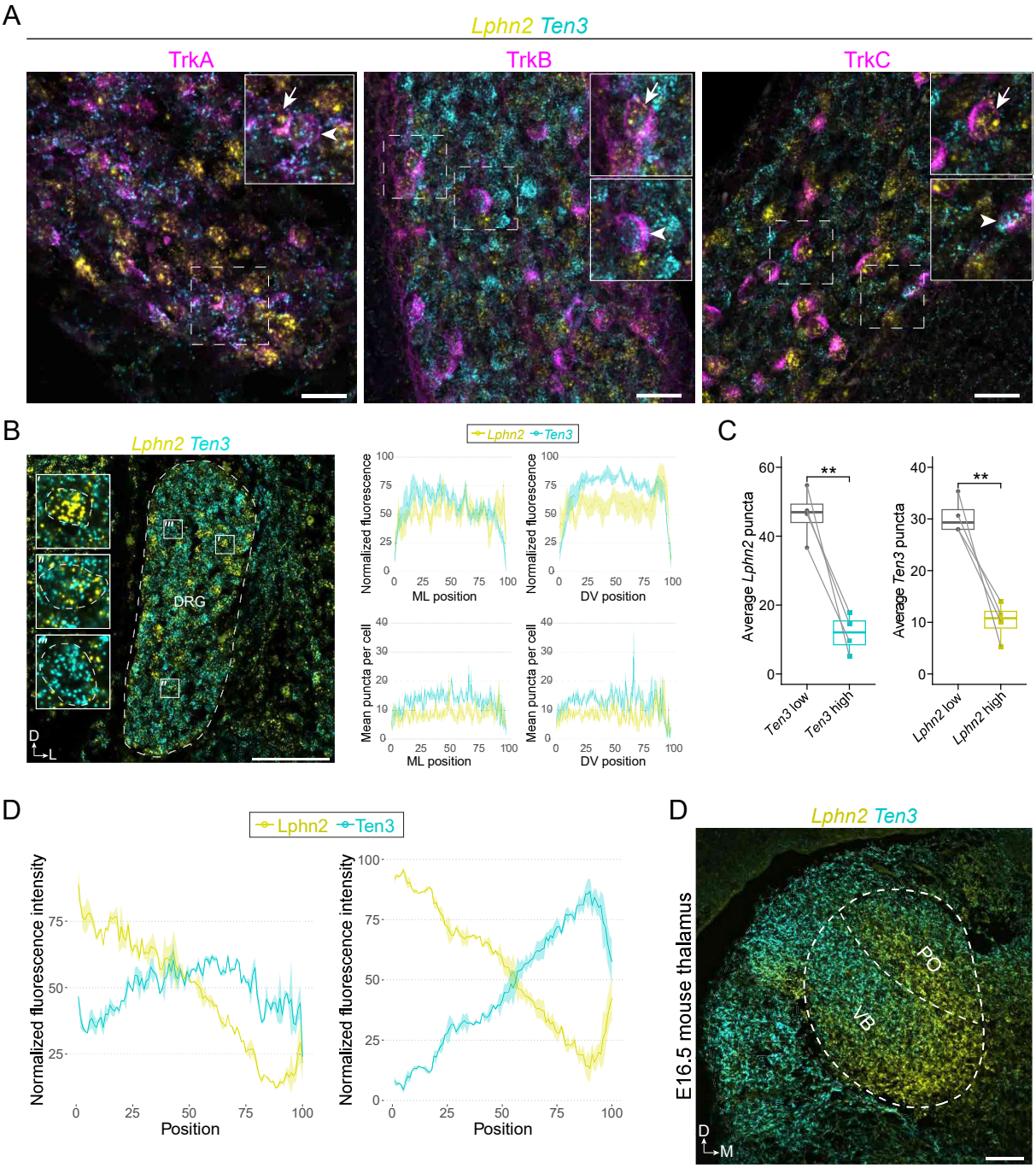
A
Lphn2 Ten3
TrkA
TrkB
TrkC
B
Lphn2 Ten3
DRG
D
L
Lphn2
Ten3
Normalized fluorescence
ML position
DV position
Mean puncta per cell
C
Average Lphn2 puncta
Average Ten3 puncta
**
Ten3 low
Ten3 high
Lphn2 low
Lphn2 high
D
Lphn2
Ten3
Normalized fluorescence intensity
Position
D
Lphn2 Ten3
E16.5 mouse thalamus
PO
VB
D
M

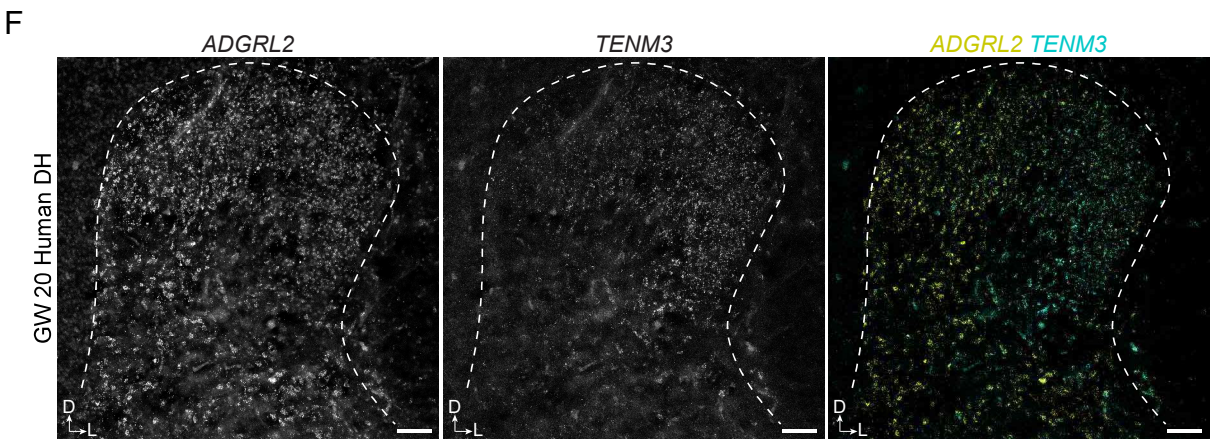
F
ADGRL2
TENM3
ADGRL2 TENM3
GW 20 Human DH
D
L

Figure S2

A

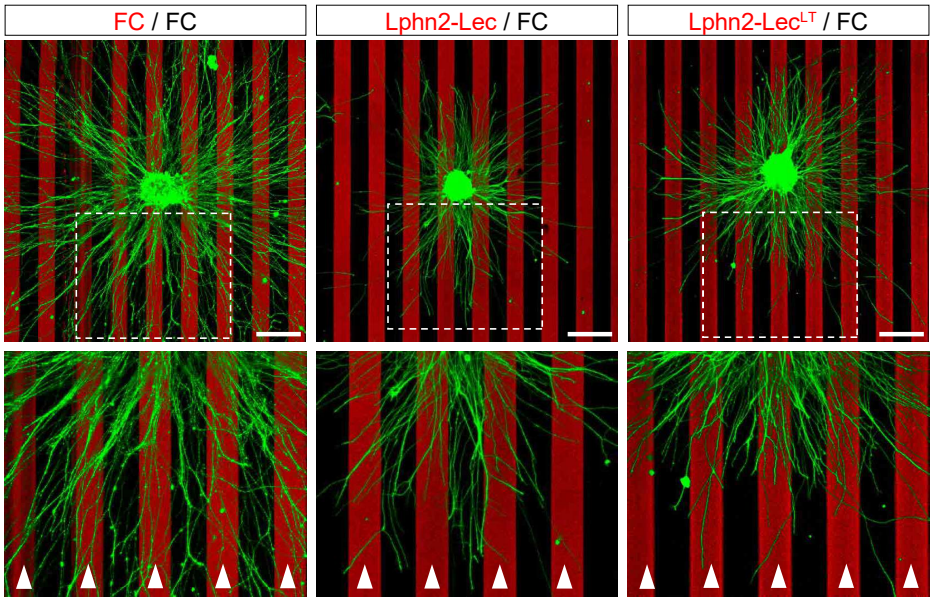

B

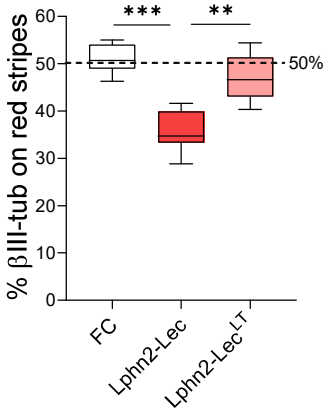

C

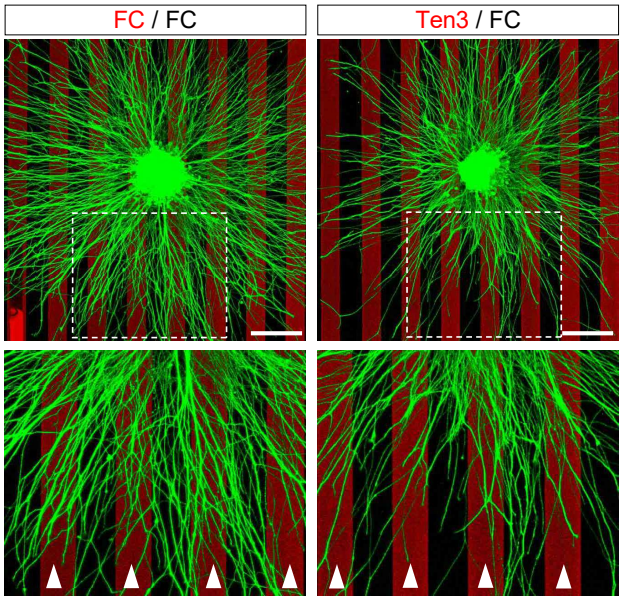

D

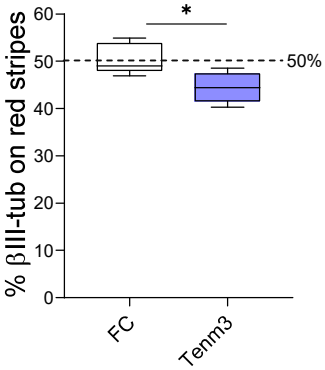

Figure S3

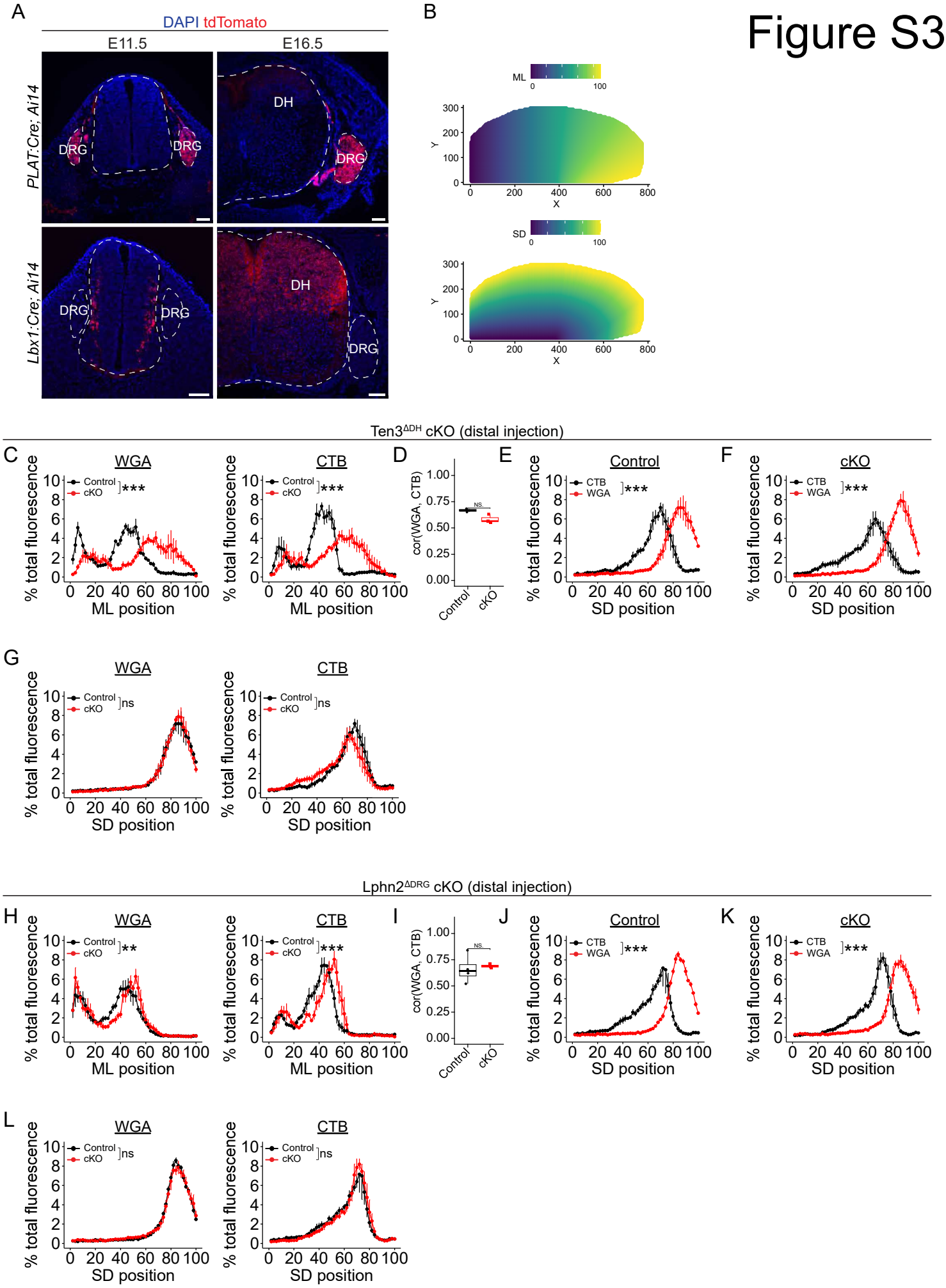
A
DAPI tdTomato
E11.5
E16.5
PLAT:Cre; Ai14
Lbx1:Cre; Ai14
DRG
DH
B
ML
SD
X
Y
Ten3ΔDH cKO (distal injection)
C
WGA
CTB
Control
cKO
% total fluorescence
ML position
D
cor(WGA, CTB)
NS.
E
F
CTB
WGA
SD position
G
ns
Lphn2ΔDRG cKO (distal injection)
H
I
J
K
L

Ten3$^{\Delta DH}$ cKO (proximal injection)

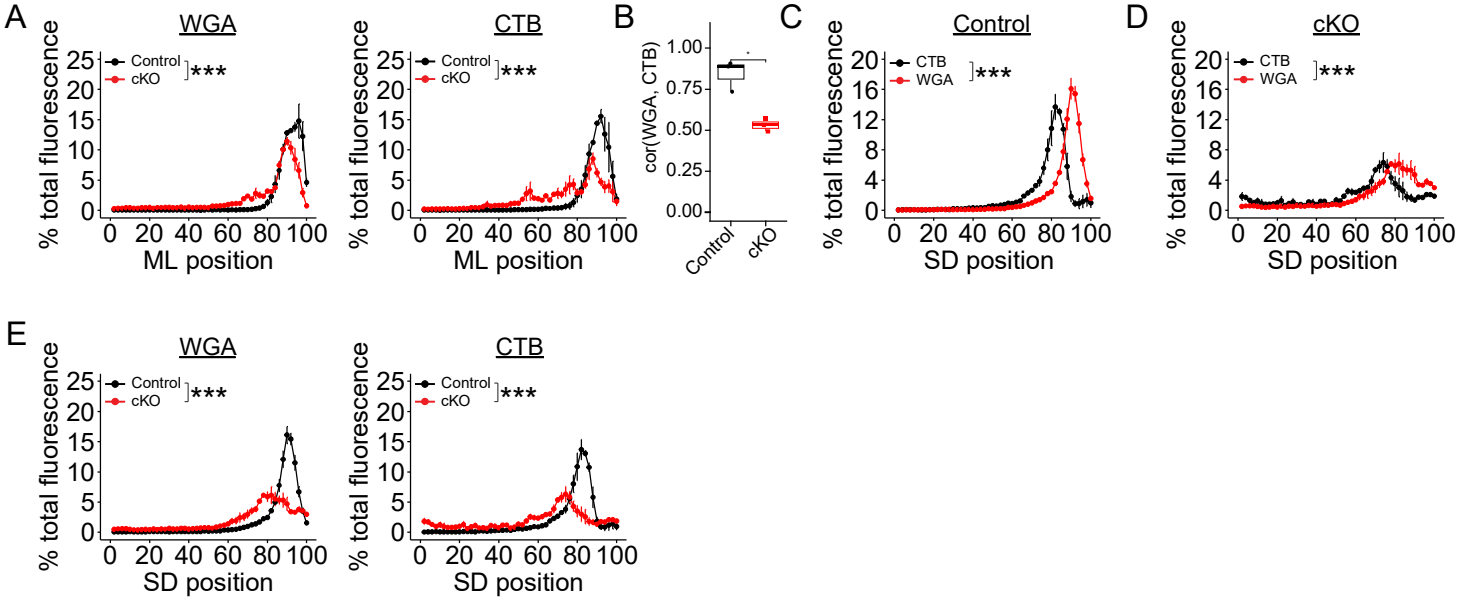

Lphn2$^{\Delta DH}$ cKO (proximal injection)

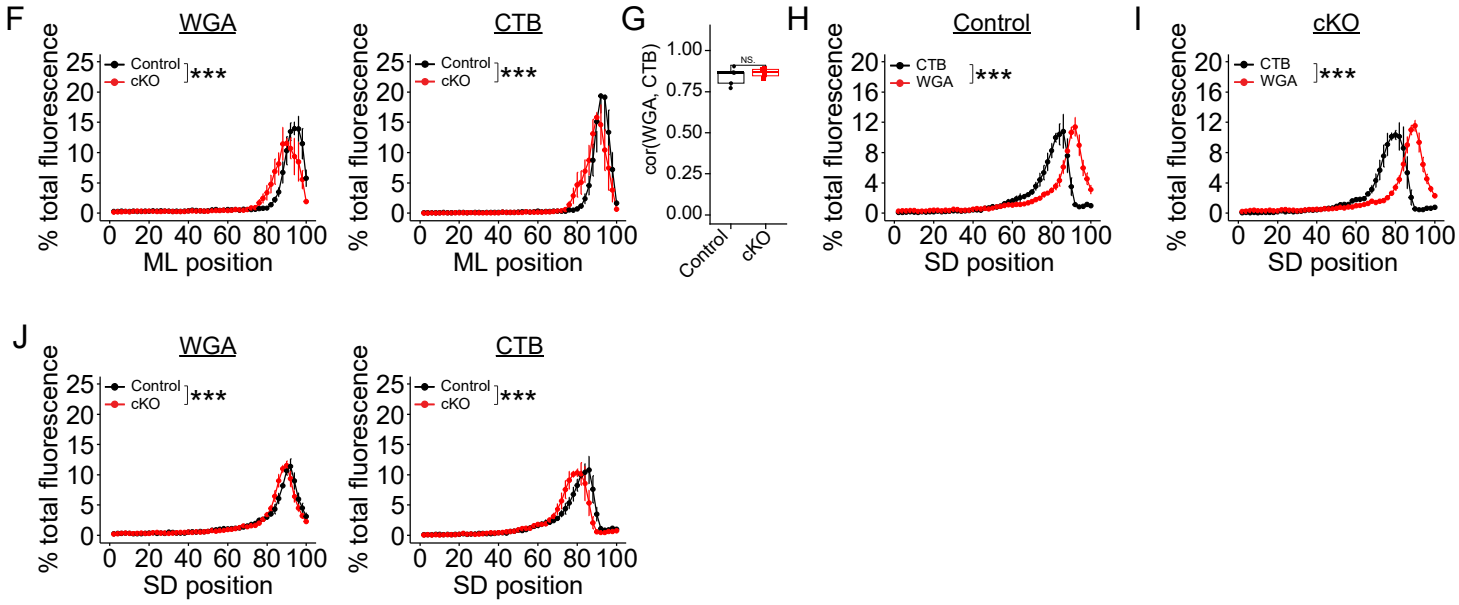

Ten3$^{\Delta DRG}$ cKO (distal injection)

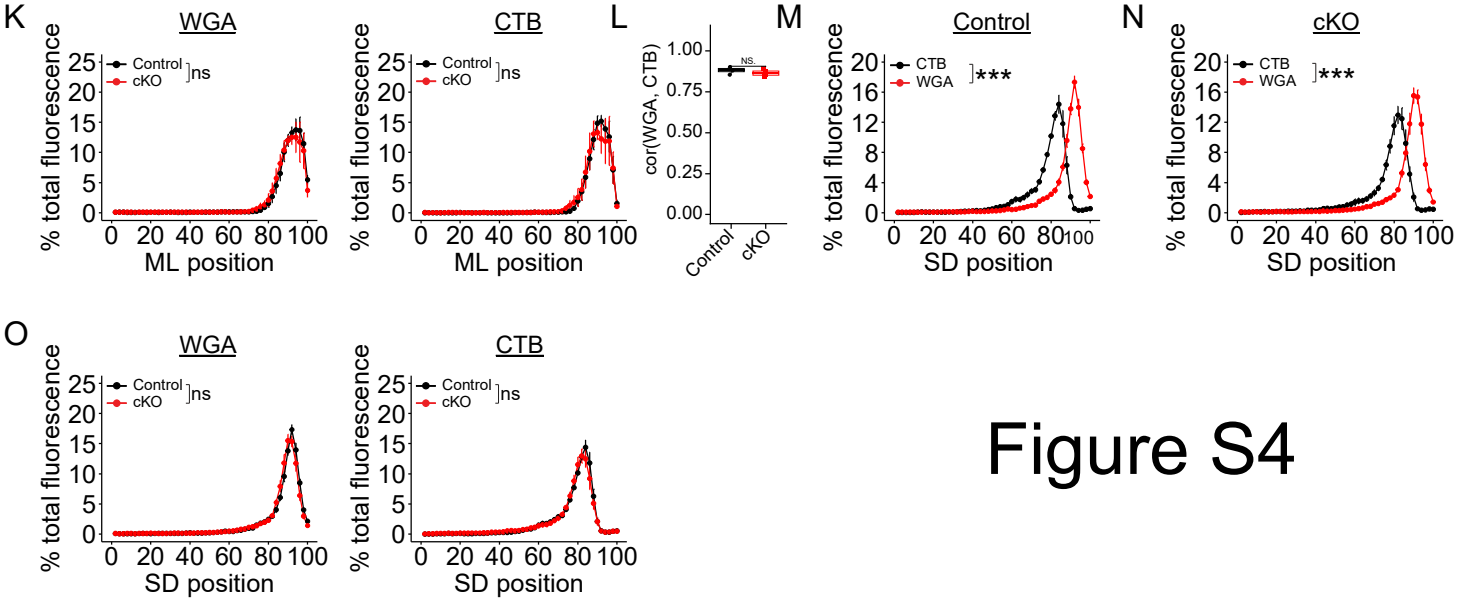

Figure S4

Figure S5

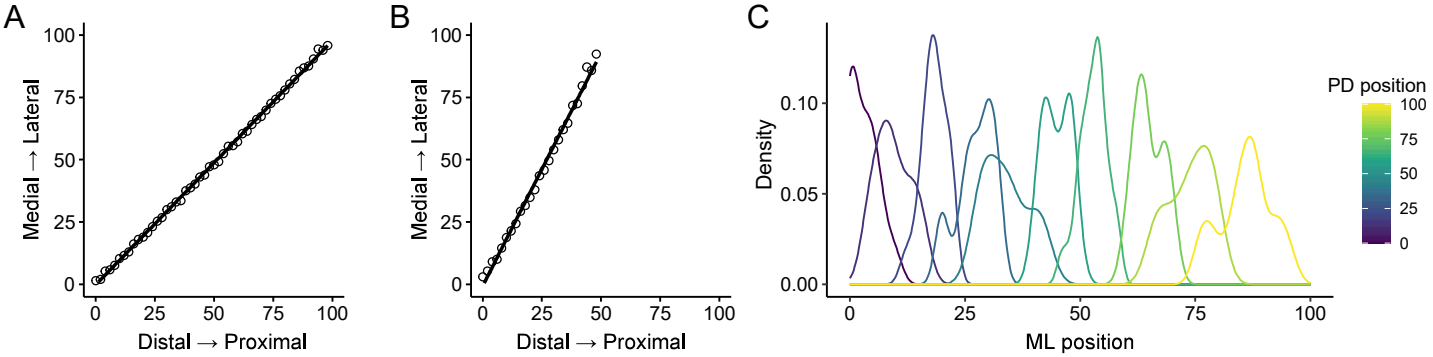
A
Medial → Lateral
Distal → Proximal
B
Medial → Lateral
Distal → Proximal
C
Density
ML position
PD position

Figure S6

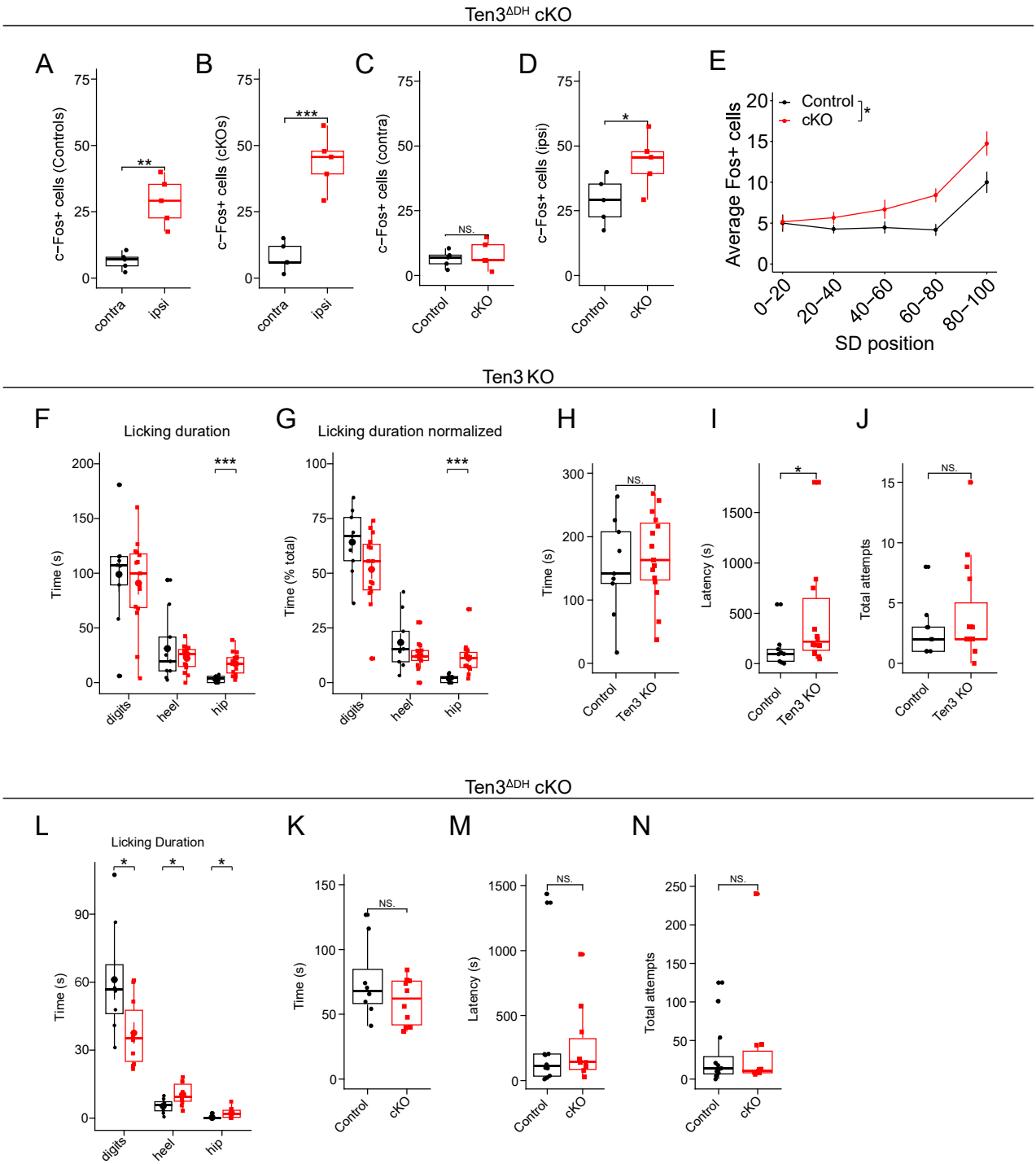
Ten3ΔDH cKO
A
c−Fos+ cells (Controls)
contra
ipsi
B
c−Fos+ cells (cKOs)
C
c−Fos+ cells (contra)
Control
cKO
NS.
D
c−Fos+ cells (ipsi)
E
Average Fos+ cells
Control
cKO
SD position
0−20
20−40
40−60
60−80
80−100
Ten3 KO
F
Licking duration
Time (s)
digits
heel
hip
G
Licking duration normalized
Time (% total)
H
Time (s)
Ten3 KO
I
Latency (s)
J
Total attempts
Ten3ΔDH cKO
L
Licking Duration
K
M
N